LBL-13860

LBL--13860

DE82 008966

DECAY STUDIES OF THE HIGHLY NEUTRON-DEFICIENT INDIUM ISOTOPES

Jan Marc Wouters

Ph.D. Thesis

February 1982

Department of Chemistry
and
Lawrence Berkeley Laboratory
University of California
Berkeley, CA 94720

DISCLAIMER

This report was prepared as an account of work sponsored by an agency of the United States Government. Neither the United States Government nor any agency thereof, nor any of their employees, makes any warranty, express or implied, or assumes any legal liability or responsibility for the accuracy, completeness, or usefulness of any information, apparatus, product, or process disclosed, or represents that its use would not infringe privately owned rights. Reference herein to any specific commercial product, process, or service by trade name, trademark, manufacturer, or otherwise, does not necessarily constitute or imply its endorsement, recommendation, or favoring by the United States Government or any agency thereof. The views and opinions of authors expressed herein do not necessarily state or reflect those of the United States Government or any agency thereof.

DISTRIBUTION OF THIS DOCUMENT IS UNLIMITED

This work was supported by the Director, Office of Energy Research, Division of Nuclear Physics of the Office of High Energy and Nuclear Physics, and by the Nuclear Sciences of the Basic Energy Sciences Program of the U.S. Department of Energy under Contract No. W-7405-ENG-48.

DECAY STUDIES OF THE HIGHLY NEUTRON-DEFICIENT INDIUM ISOTOPES

Table of Contents

Abstract

I. Introduction 1

II. Theory 7

A. Beta-decay 7

1. The interaction Hamiltonian 7

2. The beta energy spectrum (β^- and β^+) 11

3. Log ft 15

4. Electron capture 16

B. Mass formulae 18

1. Garvey-Kelson mass relations 18

2. Droplet model 24

3. Synopsis of selected formulae 30

a. Comay-Kelson 31

b. Jänecke-Eynon 32

c. Liran-Zeldes 33

d. Groote-Hilf-Takahashi 35

e. Seeger-Howard 36

f. Möller-Nix 37

III. Experimental method 41

A. Production of isotopes 42

B. Isolation of mass separated sources (RAMA) 44

1. Helium-jet 44

2. Ion source and optics 51

3. Detector chamber and tape transport 58

DECAY STUDIES OF THE HIGHLY NEUTRON-DEFICIENT INDIUM ISOTOPES

Jan Marc Wouters

Department of Chemistry, and Lawrence Berkeley Laboratory
University of California, Berkeley, CA 94720

ABSTRACT

An extension of the experimentally known nuclidic mass surface to nuclei far from the region of beta-stability is of fundamental interest in providing a better determination of the input parameters for the various nuclear mass formulae, allowing a more accurate prediction of the ultimate limits of nuclear stability. In addition, a study of the shape of the mass surface in the vicinity of the doubly-closed nuclide ^{100}Sn provides initial information on the behavior of the shell closure to be expected when Z=N=50. Experiments measuring the decay energies of $^{103-105}$In by β-endpoint measurements are described with special attention focused on the development of a plastic scintillator β-telescope coupled to the on-line mass separator RAMA (Recoil Atom Mass Analyzer). An attempt to measure the β-endpoint energy of ^{102}In is also briefly described.

The experimentally determined decay energies and

derived masses for $^{103-105}In$ are compared with the predictions of different mass models to identify which models are more successful in this region. Furthermore, the inclusion in these comparisons of the available data on the neutron-rich indium nuclei permits a systematic study of their ground state mass behavior as a function of the neutron number between the shell closures at N=50 and N=82. These analyses indicate that the binding energy of ^{103}In is 1 MeV larger than predicted by the majority of the mass models.

An examination of the Q_{EC} surface and the single- and two-neutron separation energies in the vicinity of $^{103-105}In$ is also performed to investigate further the above deviation and other possible systematic variations in the mass surface in a model-independent way. The ^{103}In Q_{EC} and the ^{105}In S_{2n} are shown to diverge seriously from systematics. Ascribing these effects to the mutual support of shell closures, which would cause a strengthening of the proton binding energy with decreasing neutron number, requires additional investigation. Interestingly, the neighboring, even cadmium 2^+ and 4^+ excited state systematics indicate that these nuclei are becoming more spherical with decreasing neutron number as expected near a double shell closure.

I. Introduction

Mass measurements of nuclei have been an integral aspect of nuclear physics research since the early investigations into the structure of the nucleus. The ground state mass (or mass excess) of a nucleus provides direct information about nuclear stability and nuclear structure. Parallel to the experimental effort to measure masses has been a strong theoretical program (Ma 76a-g) to model the mass surface. Most of the resulting theories fall into two broad catagories: the first includes models which predominantly provide accurate mass predictions for use, as an example, to calculate the limits of nuclear stability; the second includes models which, while less accurate, also provide direct insights into nuclear structure and forces.

An example from the first category includes all models based on the Garvey-Kelson (Ga 66, Ke 66, Ga 69a, Ga 69b) mass relationships. Briefly, these models relate the mass excess of a particular nucleus to a linear combination of mass excesses of nuclei within the same Z and N region, but which lie closer to the valley of β-stability. These relationships rely on the goodness of the independent-particle model of the nucleus and thus on the accuracy to which the neutron-neutron, proton-proton, and neutron-proton interactions can be averaged out.

The most notable of the latter models is that devised by Bethe and von Weizsächer (Be 36, von W 35) in which the

nucleus is considered to behave like a charged liquid drop. This simple model accurately predicts masses to 1 part in 10^4 over the known mass surface and provided an initial explanation for the binding energy systematics of nuclei lying in the valley of β-stability. Since the development of this "Liquid Drop" model, extensive modifications have been made to better describe such macroscopic features as the deformation of the mass surface, and to try to account for some of the microscopic features such as shell structure and pairing effects. Recently, several new theories have been developed which rely solely on microscopic approaches to calculate both the macroscopic and microscopic features of nuclear masses.

Evaluation of the success of these mass models relies on the availability of accurate mass excess data. These mass excesses are determined experimentally via the measurement of mass differences by mass spectroscopy, reaction Q values, or decay Q values. Mass spectroscopy, in which the difference between mass doublets or triplets is measured or the new technique in which a nuclear recoil's time-of-flight is measured along a premeasured distance, has been used extensively for the mass excess determination of stable and long lived isotopes, but has only recently been employed for the mass excess determination of short lived isotopes (Th 75, Ep 79, Vi 80). Reaction Q value measurements have been a rich source of information about

ground and excited state mass excesses especially for light nuclei reasonably distant from the valley of β-stability [e.g. ^{8}He (Ce 74)]. These multinucleon transfer reactions such as (p,^{4}He), (^{3}He,^{6}He), and (^{4}He,^{8}He) can provide quite accurate (<50keV) mass data for both particle-unbound as well as particle-bound exotic nuclei. Recently, the advent of intense pion beams has led to their successful utilization for mass measurements via double charge exchange, as has been demonstrated for ^{18}C using the reaction ^{18}O($^{-}\pi$,$^{+}\pi$)^{18}C (Se 78).

For most heavier nuclei far from the valley of stability the most prevalent method used for determining mass excesses relies on measuring the Q value associated with beta, alpha or β-delayed particle decay. β-spectroscopy was one of the original techniques used for measuring mass excesses of nuclei far from the valley of β-stability and has been intimately involved in unravelling the complexities of the weak interaction. The measurement of α-decay energies has related the ground state mass excesses of numerous nuclei in the three regions known to possess extensive α-emitting chains. β-delayed particle spectroscopy (Be 79, Ay 81) has been used in the study of isospin and its application to mass theories through the Isobaric Multiplet Mass Equation (IMME), first suggested by Wigner (Wi 57). More recently, β^{+}-particle coincidence experiments have measured the energy dependent EC/(β^{+} + EC)

ratio for β-delayed particle decays which provides reference masses for several of the α-decay chains (Pl 79).

Applying the techniques just described to investigate nuclei far from the valley of β-stability becomes very difficult because of the copious production of nuclides closer to stability. A great deal of effort has been devoted to devising experimental methods which provide A and/or Z separated radioactive samples, such as fast chemistry procedures, mass separation techniques (both off and on-line), as well as many others. The greatest advances have been made in the use of on-line mass separators because of their ability to provide mass separated samples of very short-lived nuclei ($t_{1/2} \sim 100$ ms) for investigation. Two basic designs of ISOL (Isotope Separator on Line) systems are used to provide mass separation and varying degrees of Z separation. The first, exemplified by the ISOLDE separator at CERN (Ra 76), employs an integrated target-ion source system in which the radioactive recoils diffuse out of the target into an ion source in which they are ionized and subsequently accelerated for mass separation. Z separation is achieved by employing the selective diffusion of specific elements out of the targets into the ion source. The second, exemplified by the RAMA (Recoil Atom Mass Analyzer) separator at the Lawrence Berkeley Laboratory (Mo 80a, Mo 80b, Mo 81a), employs a helium-jet to transport the recoils to the ion source. The use of light and heavy ion

fusion reactions provides partial Z selection. Many variations of these two basic systems have been built and several review articles have recently been published which describe in greater detail the development of on-line mass separators and the numerous physics problems which are currently being addressed (Ha 79, Ra 79, Ha 81, Jo 81).

Initial experiments using RAMA investigated the application of IMME to isospin quintets (Ay 79, Mo 79a, Ay 81) and demonstrated the capabilities of the then new isotope separator. These studies have since been expanded to include mass measurements using β-endpoint determinations near the predicted doubly magic nucleus ^{100}Sn (See figure 1-1). The mass surface in this region is especially interesting because of the expected increased stability of ^{100}Sn. Extensive investigations have recently been conducted in this region to map out the ground state mass surfaces and some of the excited state systematics. New mass excess data will determine whether ^{100}Sn is bound to particle decay and provide a further test of the many mass theories. In addition, examination of the mass surface in both the Z and N directions will determine if the neutron-proton shell closure reinforcement observed near ^{208}Pb is present at ^{100}Sn (Sc 79). This question is very intriguing because of its non-observance in the indium isotopes near the doubly magic nucleus ^{132}Sn (See section V).

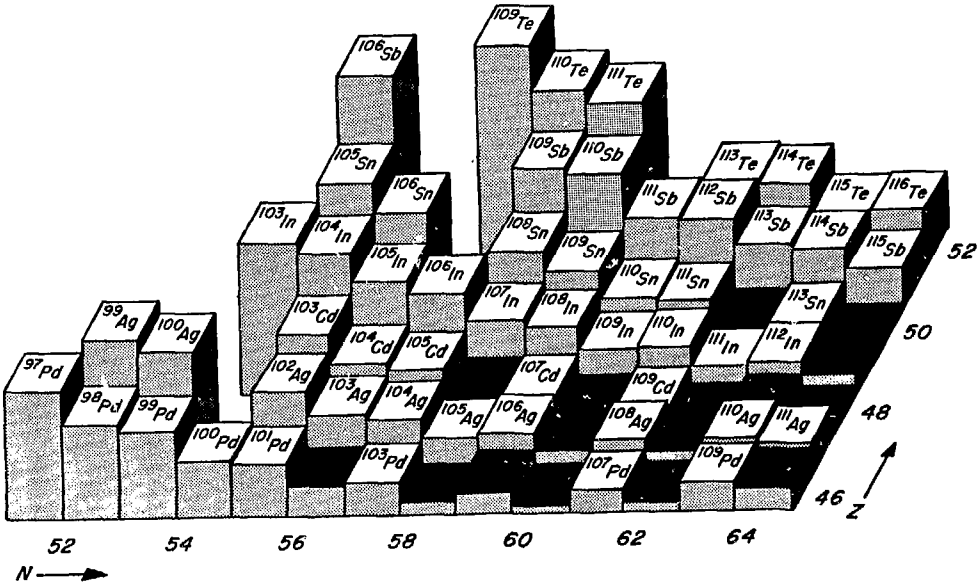

Figure 1-1. The relative mass excess for the proton rich nuclei near the Z = 50 proton shell closure. Nuclei indicated in black are stable to beta decay.

II. Theory

We begin this chapter with a review of the simple theory of β-decay. No attempt is made to derive rigorously the form of the β-interaction; however an understanding of the form of the Fermi and Gamow-Teller interactions plus their associated selection rules is presented in so far as they pertain to the endpoint analysis of β-spectra. The chapter concludes with a discussion of several selected mass theories. This latter section is subdivided into a discussion of the Garvey-Kelson relationship and the Droplet model, both of which have strongly influenced the formulation of many recent mass theories. Finally the important features, which distinguish the mass theories selected for the discussion of the experimental results, are described.

A. Beta-decay

1. The interaction Hamiltonian

The β-decay of a nucleus may be written in the symmetrical form given by equation (2-1) which suggests

$$n + \nu \rightleftharpoons p^{+} + e^{-} \qquad (2\text{-}1)$$

that the decay process can be visualized as the simultaneous transformation of a neutron into a proton and a neutrino into an electron or vice-versa. This transformation can be expressed mathematically as (Wu 66, Ma 69)

$$\mathcal{H} = g \Sigma C_i \mathcal{H}_i \tag{2-2}$$

$$= g \Sigma C_i (\Psi_p^* Q^+ O_i \Psi_n)(\Psi_e^* O_i \Psi_\nu) \tag{2-3}$$

$$+ \text{ Hermitian conjugate}$$

$$\Sigma |C_i|^2 = 1$$

where C_i are the dimensionless coupling constants (g contains units), O_i is a generalized operator which satisfies Dirac's relativistic wave mechanics for spin 1/2-particles and Q^+ is the operator which changes a neutron into a proton (Q^- performs the inverse operation). If all possible forms of the β-interaction are included, O_i may take on five different forms which are classified according to their transformation properties: scalar, vector, tensor, axial vector, and pseudoscalar. Furthermore, each of these terms possesses a parity nonconserving contribution as well as a parity conserving contribution. With the inclusion of lepton conservation a total of 35 independent coefficients are obtained which must be measured experimentally to determine the relative strength of the different contributions (Li 62). Fortunately, inclusion of the experimental results which support time reversal invariance and lepton conservation leaves only 9 independent coefficients. These may be further reduced to just the original 5 mentioned above with the use of the 2 component theory of the neutrino which states that the neutrino has negative helicity and the antineutrino has positive

helicity. Experimental results from electron-neutrino angular correlation studies indicate that the actual form of the interaction normally comprises only the vector and axial vector interactions. Thus, the β-interaction Hamiltonian is written as

$$
\begin{aligned}
&= g\{C_V(\Psi_p{}^* Q^+ \Psi_n)(\Psi_e{}^* \Psi_\nu) \\
&\quad + C_A \sum_\mu (\Psi_p{}^* Q^+ \sigma_\mu \Psi_n)(\Psi_e{}^* \sigma_\mu \Psi_\nu)\} \\
&\quad + \text{ Hermetian conjugate}
\end{aligned}
\tag{2-4}
$$

where σ_μ refers to the Pauli spin matricies. Comparison of Q^+ with the isospin operators T_x, T_y, and T_z reveals that Q^+ is just the isospin raising operator T^+ (We 66, Sh 74) where

$$
\begin{aligned}
T^+|n\rangle &= (1/2)(T_x + iT_y)|n\rangle = |p\rangle \\
T^+|p\rangle &= 0 \\
T^-|p\rangle &= (1/2)(T_x - iT_y)|p\rangle = |n\rangle \\
T^-|n\rangle &= 0
\end{aligned}
\tag{2-5}
$$

Before examining the β-decay selection rules associated with the two terms in equation (2-4) we make the following approximation. The electron and neutrino wave functions can be described as plane waves since the nuclear potential affects them only weakly (Ma 69). Furthermore, the deBroglie wavelengths of both leptons are much larger than the spatial extent of the nucleus over which the integration

in equation (2-4) is performed. Thus the wave functions for both the electron and neutrino can be expanded as a power series about the origin and just the first term, of value one, for each retained

$$H_{fi} = g\Psi_e^*(0)\Psi_\nu(0)F(Z,w)M_{fi} \cong gM_{fi} \qquad (2\text{-}6)$$

$$|M_{fi}|^2 = \{|C_V|^2/(2J_i+1)\}\sum_{fi}|\Psi_f\sum_k T^{\pm}(k)\Psi_i|^2$$
$$+ \{|C_A|^2/(2J_i+1)\}\sum_{fi}\sum_\mu|\Psi_f\sum_k T^{\pm}(k)\sigma_\mu(k)\Psi_i|^2$$
$$= |C_F|^2|M_F|^2 + |C_{GT}|^2|M_{GT}|^2$$
$$C_V = C_F \qquad C_A = C_{GT}$$

[In equation (2-6) the factor $F(\pm Z,w)$ has been added to correct for the distortion of the electron wave function caused by the nuclear charge (see next section).]

The selection rules are now easily evident from the spin dependence of the leptonic wave functions. The first term (vector) in equation (2-4) requires that the two nuclear wave functions have the same spin, $\Delta J = 0$. That is, the electron and antineutrino in the case of β^- decay or the positron and the neutrino in β^+ decay must be emitted with antiparallel spins. (The long wavelength assumption also leads to the result that neither lepton can carry away orbital angular momentum, $l=r\times p$, since r, the location at which the leptons are created in the nucleus is on the order of a Fermi and l is therefore much less than $\hbar$). In addition, the parities cannot change since the initial and

final nuclear states are of definite parity and because the leptonic wave functions are independent of position within the nucleus from the long wavelength approximation. The second term (axial vector) allows leptonic wave functions with different spin projections to contribute to the decay probability, $\Delta J = 0, \pm 1$. Thus the electron and antineutrino, and the positron and neutrino are emitted with parallel spins. The parity again cannot change. These conclusions, which are summarized in figure 2-1, correspond to the original results of Fermi, and of Gamow and Teller (Fe 34, Ga 36). The form of the β-interaction Hamiltonian presented above is limited in application to superallowed and allowed decays only.

2) The β-energy spectrum. (β^- and β^+)

The weakness of the β-interaction permits the transition probability for an electron with kinetic energy E and momentum p to be calculated using Fermi's Golden rule number 2 which can be derived from time dependent perturbation theory (Wu 66, Sh 74, Ba 77, Se 77)

$$N(w)dw = (2\pi/\hbar)(dn/dw_o)|H_{fi}|^2 \qquad (2\text{-}7)$$
$$= (m^5c^4/2\pi^3\hbar^7)g^2F(\pm Z,w)|M_{fi}|^2(w_o-w)^2pwdw \quad \text{for } e^{\pm}$$
$$w = E + m_ec^2$$

where dn/dw_o is the density of final states around the endpoint energy w_o. The factor $(w_o-w)^2pw$ arises from

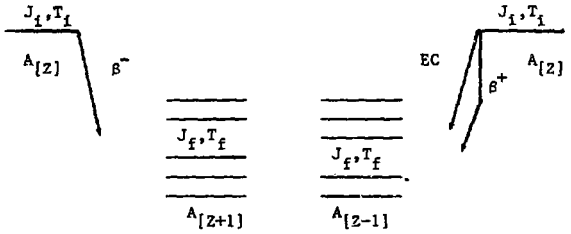

$$\Delta E^{(\beta-)} = [M(Z,A)-M(Z+1,A)]c^2 \qquad \Delta E^{(\beta+)} = [M(Z,A)-M(Z-1,A)-2M_e]c^2$$

$$\Delta E^{(EC)} = [M(Z,A)-M(Z-1,A)]c^2$$

Energy Spectrum:

$$\beta^-/\beta^+ \qquad N(w)dw = \frac{G^2}{2\pi^3}\,\frac{m_e c^2}{\hbar}\,|M_{fi}|^2\,F(\mp Z, w\pm v_o)S(w,v_o)(w_o-w)^2 pw dw$$

$$\text{EC} \qquad N(w)dw = \frac{G^2}{\pi^2}\,\frac{m_e c^2}{\hbar}\left(\frac{Z\,e^2}{\hbar c}\right)^3 |M_{fi}|^2\,(w_o-\varepsilon_k)^2 S\left[w-(w_o-\varepsilon_k)\right]$$

Log ft:

$$\beta^-/\beta^+ \log \underline{ft} = \frac{\tau_o \ln 2}{|M_{fi}|^2} \qquad f(w_o,Z) = \int_{m_e c^2}^{w_o} F(\mp Z, w\pm v_o)S(w,v_o)(w_o-w^2)pw dw$$

$$\text{EC} \quad \log \underline{f_k t} = \frac{\tau_o \ln 2}{|M_{fi}|^2} \qquad f_k(w_o,Z) = 4\pi\left(\frac{Z\,e^2}{\hbar c}\right)^3 (w_o-\varepsilon_k)^2$$

Selection Rules (Super-allowed and Allowed Decays: log $\underline{ft} \cong 2.9 - 6.0$)

Fermi Interaction :

$\Delta J = 0$
$\Delta T = 0$
No parity change

Gamow Teller Interaction :

$\Delta J = 0, \pm 1 \qquad 0 \rightarrow 0$
$\Delta T = 0, \pm 1 \qquad 0 \rightarrow 0$
No parity change

Figure 2-1. Outline of β-decay including: energy (mass) relations, electron (positron) energy spectrum expressions, log ft equations and selection rules governing Fermi and/or Gamow-Teller transitions. (See text for details).

statistical considerations governing the partitioning of the available decay energy between the electron (positron) and antineutrino (neutrino). This term, along with the energy dependent Fermi function, F, governs the shape of the β-spectrum since the interaction matrix element, M_{fi} ,is dependent only on the initial and final nuclear wave functions as has been shown. The form of equation (2-7) leads to the interesting conclusion that if the energy spectrum N(w) of a superallowed or allowed decay is plotted as

$$\{N(w)/[F(\pm Z,w)pw]\}^{1/2} \quad \text{vs} \quad (w_o-w) \qquad (2\text{-}8)$$

a linear graph [Fermi-Kurie plot (Ku 36)] should result with an abscissa intercept equal to the endpoint energy w_o.

A prerequisite for a β-endpoint analysis based on this technique is a knowledge of the Fermi function, $F(\pm Z,w)$ which is defined as:

$$F(\pm Z,w) = |\Psi_e(0)|_Z^2/|\Psi_e(0)|_{Free}^2 \qquad (2\text{-}9)$$

To properly treat the electron wave function in the vicinity of the nucleus, relativistic wave functions should be used. The Dirac equation defines the wave functions properly, but unfortunately produces an infinity at r=o. To circumvent this problem the integral $|\Psi_e(0)|_Z^2$ is replaced by $|\Psi_e(R)|_Z^2 V_n$

where R and V_n are the nuclear radius and nuclear volume, respectively (Bl 52). This approximation assumes that the electron wave function is approximately constant within the nucleus which is equivalent to the long wavelength assumption made previously. One additional factor accompanying $F(\pm Z,w)$, $S(w,w\pm v_o)$, corrects for the screening of the nuclear charge by the atomic electrons (Ko 65). (The quantity v_o describes the change in the nuclear potential due to the screening.) The Fermi function with the screening correction can then be written for superallowed and allowed decays as:

$$F(\pm Z,w\mp v_o)S(w,w\mp v_o) \text{ for } e^{\pm} \tag{2-10}$$

$$F(\pm Z,w') = 2(1-\gamma_o)(2p'R/\hbar)^{-2(1-\gamma_o)}e^{\pi\nu}|\Gamma(\gamma_o+i\nu)^2$$
$$\times[\Gamma(2\gamma_o+1)]^{-2}$$
$$w' = w\mp v_o$$
$$\gamma_o = [1-(\alpha Z)^2]^{1/2}$$
$$\alpha = e^2/\hbar c$$
$$\nu = \pm\alpha Z(w')/cp'$$
$$S(w,w\mp v_o) = \{[(w\mp v_o)^2-m_ec^2]/[w^2-m_ec^2]\}^{1/2}$$
$$\times\{(w\mp v_o)/w\}$$
$$v_o = 1.13\alpha^2Z^{4/3}m_ec^2$$

The decay probability for a given decay energy, w, may now be expressed as (Se 77):

$$N(w)dw = (G^2/2\pi^3)(mc^2/\hbar)|M_{fi}|^2 F(\pm Z, w\mp v_o) S(w, w\mp v_o) \times (w_o - w)^2 pwdw \text{ for } e^{\pm} \qquad (2\text{-}11)$$

$$G = (g/mc^2)(mc/\hbar)^3$$

where G is a dimensionless constant.

3) Log ft

The strong energy dependence of the statistical factor presents problems when comparing matrix elements, M_{fi}, using λ, the probability per unit time of emission of a β particle [see equation (2-12a)], in order to classify different decays. This difficulty may be resolved by constructing a new function ft as in equation (2-12b) (Ma 69):

$$\lambda = \int_{m_e c^2}^{w_o} N(w)dw = \{|M_{fi}|^2/\tau_o\} f(w_o, Z) \qquad (2\text{-}12a)$$

$$\tau_o = (2\pi^3/G^2)(\hbar/mc^2)$$

$$f(w_o, Z) = \int_{m_e c^2}^{w_o} F(\pm Z, w\mp v_o) S(w, w\mp v_o)(w_o - w)^2 pwdw$$

$$ft = f(w_o, Z) t_{1/2} = f(w_o, Z) \ln 2/\lambda \qquad (2\text{-}12b)$$

$$= \tau_o \ln 2/|M_{fi}|^2$$

Since the half-life $t_{1/2}$ is measurable and $f(w_o, Z)$ can be calculated knowing only the endpoint energy, calculation of ft provides a determination of $|M_{fi}|^2$. The wide variation in the observed ft for all beta decays, approximately 20 orders of magnitude, makes use of the function log ft more convenient than ft for classifying different decays (see

figure 2-1). For superallowed and allowed decays the log ft usually varies from 3.0 to 6.5. From Table 2-1, which presents the spin assignments for the initial and final states, the spin change and log ft for the nuclei used to calibrate the β-telescope and the studied indium isotopes, all the decays are inferred to be allowed. [The large log ft observed for the β^+ decay of ^{66}Ga results from the pure Fermi decay being isospin forbidden, ($\Delta T=1$). This effect leads to a slight deviation of the β-energy spectrum from the normal statistical shape which can be safely ignored for these experiments (Ca 63).

4) Electron capture:

All nuclei studied in this work decay by positron emission and so a brief description of the competing electron capture process is now presented. The fundamental differences between positron emission and electron capture are that in electron capture all neutrinos are emitted with the total decay energy w_o and there exists no energy threshold. To account for these differences equation (2-11) must be modified, substituting the appropriate atomic orbital as the electron wave function for the statistical factor describing the sharing of the decay energy between the positron and neutrino. For the studied indium isotopes the ratio $\lambda_{EC}/\lambda_{\beta^+}$ is about 10%. This contribution does not in anyway affect the β^+ energy spectrum, but does change the log ft since the total transition probability $\lambda_{EC} + \lambda_{\beta^+}$

Table 2-1. Initial and Final Spins and log *ft* Values for All Nuclei Used or Observed in These Experiments

Nucleus	J_{Init}	J_{Final}	ΔJ	$\Delta\pi$	log *ft*
^{38}K a)	3^+	2^+	1	No	5.0
^{62}Cu a)	1^+	0^+	1	No	5.2
^{66}Ga a)	0^+	0^+	0	No	7.9
^{123}Cs b)	$1/2^+$	$3/2^+$	1	No	5.6
^{124}Cs a)	(1^+)	2^+	1	No	5.1
^{102}In c)	(5)	4^+	1	?	(5.6)
^{103}In d)	$9/2^+$	$7/2^+$	1	No	4.9
^{104}In e)	5^+	4^+	1	No	6.0
^{105}In f)	$9/2^+$	$7/2^+$	1	No	5.8

a) Spins and log *ft* taken from *7th ed Table of Isotopes*, (Le 78).

b) Spins and log *ft* taken from (Ma 81).

c) Spins and half-life taken from (Be 81). Log *ft* calculated using the Comay-Kelson (Ma 76e) mass predictions, to determine the masses of ^{102}In and ^{102}Cd, and the log *ft* tables of Gove and Martin (Go 71).

d) Spins taken from (Be 81a). Log *ft* calculated using tables of Gove and Martin (Go 71).

e) Spins and half-life taken from (Hu 78). Log *ft* calculated using tables of Gove and Martin (Go 71).

f) Spins and half-life taken from (Wi 80). Log *ft* calculated using tables of Gove and Martin (Go 71). Branching ratios corrected for internal conversion using the theoretical tables of Rösel et al. (Ro 78) and by assuming an M1 multipolarity for all transtions. (The log *ft* is 5.8 if the internal conversion contribution is ignored.)

determines the log ft to a particular state.

B) Mass formulae

The Garvey-Kelson mass relations and the Droplet model illustrate the two main objectives of mass formulae: calculating accurate mass predictions and representing the nuclear mass surface theoretically. These objectives are most important when extrapolations are made far from the mass region where the free parameters of the formulae are defined. Some models which calculate the known mass excesses more poorly than the Garvey-Kelson mass relation approaches can occasionally be extrapolated long distances, especially for heavy masses, with higher accuracy because of their theoretical treatment of general trends which is lacking in the Garvey-Kelson approaches (So 71). This point becomes increasingly important as mass formulae attempt to duplicate more subtle trends of experimental masses [e.g. the mutual support of magicities (shell closures) and the separation of the two odd-A mass surfaces]. The general direction of newer mass formulae is to combine the two objectives by including mass relations and models together [e.g. Jänecke-Eynon (Ma 76g)] or by constructing more detailed theoretical models. [See articles by Zeldes for more details (Ze 80, Ze 81)].

1) Garvey-Kelson mass relations

Several mass relationships have been introduced over the last two decades which relate the ground state mass of a

nucleus far from the valley of β-stability to those of neighboring nuclei lying nearer to stability. The best known relationships were formulated by Garvey and Kelson (Ga 66, Ke 66) and are based on the independent-particle model of the nucleus. Such a model incorporates the two body interactions (i.e., n-n, p-p and n-p) into the single particle energies with any residual interactions assumed to be between nucleons in the same shell level (see below) (Ga 66). Without introducing any specific assumptions about the nuclear Hamiltonian other than that the interaction matrix elements vary slowly with A, the mass relationships may be constructed as a set of difference equations

$$\sum_i^{\alpha} C_i M(N+\Delta N_i, Z+\Delta Z_i) = 0 \qquad |C_i| = 1 \qquad (2\text{-}13)$$

where M refers to the mass excess associated with nucleus i and which include the following constraints that insure that the sum of two-body interactions vanishes

$$\sum_i^{\alpha} N_i C_i = 0 \qquad \sum_i^{\alpha} Z_i C_i = 0 \qquad \sum_i^{\alpha} N_i Z_i C_i = 0 \qquad (2\text{-}14)$$

no N=Z=odd nuclei, $N \geq Z$

Two nontrivial forms of equation (2-13) first occur with $\alpha=6$ (Ga 69a, Ga 69b)

$$M(A,T_Z+2)-M(A,T_Z)+M(A-1,T_Z+1/2)-M(A-1,T_Z+3/2) \qquad (2\text{-}15a)$$
$$+M(A+1,T_Z+1/2)-M(A+1,T_Z+3/2) \qquad \text{Transverse}$$

$$M(A+4,T_Z)-M(A,T_Z)+M(A+1,T_Z+1/2)-M(A+3,T_Z+1/2) \qquad (2\text{-}15b)$$
$$+M(A+1,T_Z-1/2)-M(A+1,T_Z-1/2) \quad \text{Longitudinal}$$

and are represented graphically in figure 2-2a. The most general forms of M(N,Z) that satisfy equations (2-15a) and (2-15b) are

$$M(N,Z) = g_1(N) + g_2(Z) + g_3(N+Z) \qquad (2\text{-}16a)$$

and

$$M(N,Z) = f_1(N) + f_2(Z) + f_3(N-Z) \qquad (2\text{-}16b)$$

respectively, where g_i and f_i are arbitrary functions of their arguments. Comparison of the masses derived from equation (2-15a) or equation (2-15b) with measured masses indicates that the former gives a better overall fit to the mass surface (Ga 69a) and so is commonly used for the construction of mass tables. (see section II-B3b)

Figures 2-2c and d illustrate the mass relationship equation (2-15a), assuming four-fold degenerate single particle levels. This simple figure clearly shows the cancellation of n-n, p-p and n-p interactions (part c) as well as the reason for excluding odd-odd self-conjugate nuclei (part d). Furthermore, the effects of the single particle model assumption ,including the restriction of any residual interaction to nucleons within the same nuclear level, become even more evident and illustrate the resulting

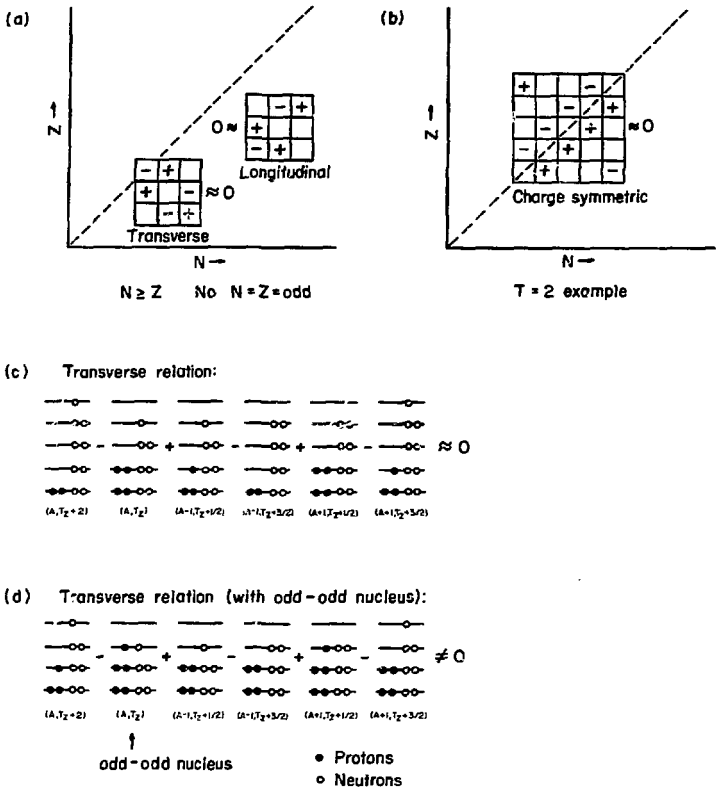

XBL821-4

Figure 2-2. Garvey-Kelson mass relations. Illustration of a) transverse and longitudinal mass relations; b) charge symmetric mass relation; c) transverse relation, using four fold degenerate single particle levels, showing approximate cancellation of n-n, p-p and n-p interactions; and d) same as c, but showing breakdown of transverse relation with inclusion of odd-odd nucleus.

limitations of the mass relationship (Ga 69a, Ga 69b). For example, the corresponding two-body interactions which must cancel occur in different nuclei and will therefore have slightly different strengths, especially the n-p interaction, due to the different radii, nuclear shapes and Coulomb energies for different A's. This effect should be most noticeable near double closed shells because the mass surface exhibits discontinuities. Furthermore, a ground state wave function cannot usually be described by a single independent-particle configuration as illustrated in figure 2-2c. Finally, the assumption is made that adjacent nuclei possess a definite parentage relationship between their ground states, which is not always the case, as is evident for ^{11}Be where the odd neutron fills the $s_{1/2}$ orbital yielding $J^{\pi} = 1/2^{+}$ as opposed to $J^{\pi} = 1/2^{-}$ which is expected from the complete filling of the $p_{1/2}$ neutron orbital in ^{12}Be (Ta 60).

The mass relationship as presented is useful for predicting individual masses and as a recursion relationship to extrapolate masses far from the valley of β-stability. A more general approach regards the M(N,Z), equation (2-16a), as a set of solutions to the set of homogeneous partial difference equations described by equation (2-15a). A unique set of solutions may be obtained from a χ^2-minimization of the differences $M(N,Z)_{G-K} - M(N,Z)_{EXP}$ (Ma 76e). In practice equation (2-17), which is equivalent

to (2-16a), is used where M is the mass excess, since one can approximately separate out the volume, Coulomb and symmetry energies leaving the residual terms g_1, g_2 and g_3 which vary smoothly about zero.

$$M(N,Z) = N\Delta M_n + Z\Delta M_H - \alpha A + \beta Z^2 + \eta(N-Z)^2 + g_1(N) + g_2(Z) + g_3(A) \qquad (2\text{-}17)$$

The coefficients α and β are arbitrarly chosen and η is fixed by the requirement that the sum of all $g_3(N+Z)$ terms equals zero.

Both mass relationships, as described, are limited in their applicability to nuclei with $N \geq Z$. This limitation can be removed with the use of a modified form of equation (2-15a) which is symmetric in T_Z (Ma 76e).

$$M(A,T_Z=-T)-M(A,T_Z=+T) = \sum_{A'=A-(2T-1)}^{A+(2T+1)} [M(A',-1/2)-M(A',+1/2)] \qquad (2\text{-}18)$$

This expression assumes that nuclear forces are charge independent to estimate the mass of a proton rich nucleus $M(A,-T_Z)$ from its neutron rich mirror $M(A,T_Z)$. The Coulomb energy difference is approximated by summing an appropriate number of $M(A,T=1/2)$ mass differences across the N=Z line. (See figure 2-2b for an illustration of the $T_Z=-2$ case). Combined use of equation (2-15a) and (2-18) to determine the

masses of $T_Z = -1/2$, and $T_Z \geq 1$ nuclei has enabled mass predictions of proton rich nuclei up to A=70 and $T_Z = -5/2$ (Ma 76e).

Approximately 5000 masses have been predicted by the most recent many parameter, χ^2-minimization using the basic Garvey-Kelson mass relations with a resulting standard deviation between experimental and calculated masses of 118 keV for the neutron rich nuclei and 100 keV for the proton rich nuclei (Ma 76e).

2) Droplet model

The ideal theoretical representation of the mass surface should be based on first principles. Such a description, which would permit the calculation of all nuclear properties, does not exist presently because of our incomplete understanding of nuclear forces. An alternative interim solution is to recognize that the saturation of nuclear forces leads to the expectation that a major part of the nuclear binding energy can be expressed as a series expansion in powers of $A^{-1/3}$. In addition, important features which result from the independent-particle nature of the nucleus (e.g. shell closures and even-odd A mass surfaces) should also be included. A natural solution is to superimpose an approximate microscopic theory on top of a macroscopic theory to describe the general features as well as some details of the mass surface (St 67)

$$M(N,Z) = M_H Z + M_N N + \text{Macroscopic term} + \text{Microscopic term} \quad (2\text{-}19)$$

Macroscopic = Liquid drop model or Droplet model
Microscopic = Shell corrections + $|N-Z|$ Wigner term + odd-even term.

Equation (2-19) represents such a theory the macroscopic and microscopic parts of which will be described in this section.

The justification for representing the macroscopic features of the nucleus as a charged liquid drop is based on the leptodermous (thin skinned) nature of the nucleus (My 71). The nucleus has an approximately constant density, ρ_o, due to the saturation characteristic of nuclear forces, (proportional to $A^{-1/3}$) with just a thin skin through which the density drops from ρ_o to 0. These gross features suggest a natural division of the nuclear energy (mass) into three parts.

$$\text{Macroscopic } E = \text{Volume term} + \text{Surface term} + \text{Coulomb term} \quad (2\text{-}20)$$

The Droplet model combines this separation of the macroscopic energy [equation (2-20)] and the saturation behavior of nuclear forces to obtain a binding energy equation which is expanded in powers of $A^{-1/3}$ and I^2 [$I=(N-Z)/A$] up to second order where A (volume term) is defined as the zero order term. The remaining terms include the

original liquid drop model first order terms $A^{2/3}$ (surface term) and I^2A (volume symmetry term) which are added to the terms $A^{-1/3}$, $I^2A^{2/3}$ and I^4A (My 71). The following description of the Droplet model is based on the work of Myers and Swiatecki (My 69, My 71, My 74, My 76a, My 77).

Using the Droplet model formalism, the macroscopic portion of the binding energy may be written as

$$E = \iiint_{vol.} e + \iint_{surf.} \sigma + (1/2)e^2 \iiint_{Z_1} \iiint_{Z_2} P_{12}\rho_Z(1)\rho_Z(2)/r_{12} \qquad (2\text{-}21)$$

where e, the energy per nucleon (not to be confused with the unit of electric charge), and σ, the surface tension coefficient, are expressed as Taylor series expansions in the degrees of freedom of the nucleus. Selection of $\rho_Z(r)$ and $\rho_N(r)$, the respective nucleon densities, and Σ_Z and Σ_N, (to be discussed below) the shapes of the respective nucleon surfaces and their redefinition as dimensionless quantities, is a major contribution of the Droplet model. As redefined [equation (2-22)], these parameters are $\varepsilon(r)$, which specifies the deviation of the total density, ρ, from ρ_o, $\delta(r)$, which specifies the neutron-proton density fluctuations, Σ, which specifies the mean nuclear surface, and τ, which specifies the neutron skin thickness

$$\begin{aligned} \varepsilon(r) &= (-1/3)[(\rho(r)-\rho_o)/\rho_o] = \bar{\varepsilon} + \tilde{\varepsilon}(r) \\ \delta(r) &= [\rho_N(r)-\rho_Z(r)]/\rho(r) = \bar{\delta} + \tilde{\delta}(r) \end{aligned} \qquad (2\text{-}22)$$

$$\tau = R_N(\Sigma_N) - R_Z(\Sigma_Z) = \bar{\tau} + \tilde{\tau}$$

The ground state energy is calculated by minimizing the energy E with respect to variations in $\bar{\varepsilon}$, $\tilde{\varepsilon}$, $\bar{\delta}$, $\tilde{\delta}$ and $\tilde{\tau}$ holding the shape, Σ, fixed. A relation between $\bar{\delta}$ and $\bar{\tau}$ removes one parameter, $\bar{\tau}$, as an independent degree of freedom. The final minimized Droplet model energy is written in equation (2-23)

$$\begin{aligned} E(N,Z,\Sigma) = {} & [-a_1 + J\bar{\delta}^2 - (1/2)K\bar{\varepsilon}^2 + (1/2)M\bar{\delta}^4]A \\ & + [a_2 + (9/4)(J^2/Q)\bar{\delta}^2]A^{2/3}B_s + a_3A^{1/3}B_k \\ & + C_1Z^2A^{-1/3}B_c - C_2Z^2A^{1/3}B_r - C_5Z^2B_w \\ & + C_3Z^2A^{-1} - C_4Z^{4/3}A^{-1/3} \end{aligned} \qquad (2\text{-}23)$$

where

$$\bar{\delta} = [1 + (3/16)(C_1/Q)ZA^{-2/3}B_v]/[1 + (9/4)(J/Q)A^{-1/3}B_s]$$

$$\bar{\varepsilon} = [-2a_2A^{-1/3}B_s + L\bar{\delta}^2 + C_1Z^2A^{-4/3}B_c]/K$$

r_o = nuclear radius constant

Coefficients:

a_1 = volume energy
a_2 = surface energy
a_3 = curvature correction
J = symmetry energy
Q = effective surf. stiffness
K = compressibility
L = density symmetry
M = symmetry anharmonicity

C_1 - C_5: Coulomb Coeff.

Shape Dependences:

B_s = surface energy
B_c = Coulomb energy
B_k = curvature energy
B_r = vol. redistribution E.
B_v = neutron skin energy
B_w = surf. redistribution E.

Equation (2-23) is included for completeness to indicate the physical effects explicity accounted for by the Droplet model. A simplified version of equation (2-23) for spherical nuclei is given below, which ignores the Coulomb force and approximates $\bar{\delta}$ and $\bar{\varepsilon}$, to more clearly illustrate the physical content of the Droplet model energy formula:

$$\begin{aligned} E(Z,N) = & -a_1A+a_2A^{2/3}+JI^2A+[a_3-(2a_2{}^2/K)]A^{1/3} \\ & -[(9/4)(J^2/Q)-(2a_2L/K)]I^2A^{2/3} \\ & -(L^2/2K-M/2)I^4A \end{aligned} \qquad (2\text{-}24)$$

The original liquid drop terms are now supplemented by the additional second order terms, previously mentioned, which involve subtle balances between various forces. For example, the $I^2A^{2/3}$ term contains the quantity J^2/Q which describes the tendency of the central nucleus to increase the n-p symmetry, which decreases the bulk energy, by pushing neutrons outward at the expense of the surface energy. The validity of the Droplet model approach may be evaluated by plotting the nuclear part of the known binding energies versus $A^{-1/3}$ which equation (2-24) indicates should be linear. Experimentally, such a plot is linear down to A=50 and approximately linear from A=50 to A=10. (My 71)

The microscopic corrections, added to the macroscopic energy, can be divided into three parts: shell corrections, the "Wigner term" and the nucleon odd-even pairing energy.

Inclusion of shell corrections was developed by Strutinsky (St 67) and is essential for all macroscopic-microscopic theories. Proper normalization of the shell energies, which constitutes the primary difficulty, is accomplished by subtracting an average shell energy (e.g. summing over a continuous distribution of states) from the calculated shell energies. Myers and Swiatecki calculate a shell correction in this matter for the Droplet model by subtracting a sum over the single particle energies of a degenerate Fermi gas from a similar sum with the single particle energies bunched to create the observed shell gaps (Sw 63, My 66a, My 77). Using the magic numbers which are experimentally observed, the only degrees of freedom which are needed must specify the amount of bunching and the absolute position of the system of bunched levels; the single particle levels are linearly bunched preserving the original order and number of levels, but increasing their density by the amount of bunching. An additional multiplicative, shape-dependent term with one degree of freedom is added that reduces the shell correction with increasing deformation of the nucleus (My 66b). The final form of the shell correction is written as

$$S(N,Z,\theta) = [\Sigma\varepsilon_i(\text{bunched}) - \Sigma\varepsilon_i(\text{unbunched})] \times (1-2\theta^2)\exp(-\theta^2) \qquad (2\text{-}25)$$

The two additional microscopic corrections, the Wigner

term and the odd-even pairing term, account for the tendency of the nucleus to have equal numbers of protons and neutrons and the splitting of the mass surface into three distinct surfaces for even-even, odd-A, and odd-odd nuclei, respectively. The Wigner term arises from the increased overlap of neutron and proton wave functions in identical orbitals (My 77) and thus is proportional to the absolute value of $I = (N-Z)/A$. The odd-even pairing term is a discontinuous function ($-C/\sqrt{A}$, 0, $+C/\sqrt{A}$ for even-even, odd-A or odd-odd nuclei) which corrects for the pairing energy of the last neutron and/or proton depending upon whether the nucleus is even-even, odd-A or odd-odd.

The free parameters of the complete Droplet model plus microscopic corrections are adjusted to obtain the best overall fit to the known ground state masses and the fission barriers. Since the model is a complete model and not just a mass relation, many of the interesting nuclear observables (e.g. nuclear radii, quadrupole moments and nuclear deformations) may be calculated from it. The root mean square (rms) deviation of the calculated masses from the known masses is approximately 1 MeV (Hi 75) which is larger than the rms deviation of the Garvey-Kelson relations as expected.

3) Synopsis of selected formulae

This discussion of mass formulae concludes with a brief description of several formulae which, along with the

Garvey-Kelson (as revised by Jänecke), and the Myers-Swiatecki formulae are compared to the experimentally determined indium masses (see section V). Using the classification schemes previously mentioned, the formulae may be subdivided into a) mass relations: Garvey-Kelson [Jänecke (Ma 76e)], Comay-Kelson (Ma 76f), and Jänecke-Eynon (Ma 76g); b) microscopic theory: Liran-Zeldes (Ma 76d); and c) macroscopic-microscopic models: Myers (Ma 76a), Groote-Hilf-Takahashi (Ma 76b), Seeger-Howard (Ma 76c), and Möller-Nix (Mo 80c).

a) Comay-Kelson

The Comay-Kelson mass predictions are based on the Garvey-Kelson transverse mass relation, but eliminate the χ^2-minimization procedure (Ma 76f). Instead, a series of reference skeletons, consisting of two masses for each A, is obtained, using the known mass surface. From these skeletons a mass table is constructed by successive application of the transverse mass relation to calculate masses as far from the skeleton as desired. The errors, $\Delta M_i(N,Z)$, for each predicted mass, $M_i(N,Z)$, are estimated from the average distance between the predicted mass and the skeleton, i. The final mass, $M(N,Z)$, is calculated from a weighted average of the $M_i(N,Z)$ and the error is determined from the dispersion in the predicted masses. The localization of the calculation removes the influence of distant masses originally introduced through the global

least squares fitting procedure. In addition, unknown masses are not penalized with respect to known masses since the χ^2-minimization procedure used by Garvey and Kelson implicitly introduced zero weighting for the unknown masses.

b) Jänecke-Eynon

The Jänecke-Eynon mass formula is a generalized Garvey-Kelson mass relation which explicitly accounts for the residual neutron-proton interaction, I_{np}. The incomplete treatment of this interaction in the Garvey-Kelson formalism leads to small systematic errors which cause the transverse, GKT [equation (2-15a)], and longitudinal, GKL [equation (2-15b)], relations to diverge. Figure 2-2c illustrates how the interaction between the odd neutron-odd proton in the third and last terms does not fully cancel out (Ja 72). The Garvey-Kelson relations possess the difficulty that GKT and GKL are independent of T_z and A, respectively, which is known to be inaccurate.

Jänecke and Eynon rederive the basic Garvey-Kelson relations and explicitly include the effective neutron-proton interaction which yields two inhomogeneous difference equations analogous to the original homogenous difference equations (Ja 72, Ja 74)

$$\Sigma_T(A,T_Z) = I_{np}(A+1,T_Z+3/2)-I_{np}(A+1,T_Z+1/2) \qquad (2\text{-}26a)$$
$$\Sigma_L(A,T_Z) = -I_{np}(A+4,T_Z)+I_{np}(A+2,T_Z) \qquad (2\text{-}26b)$$

where Σ_T and Σ_L refer to the homogeneous Garvey-Kelson

difference relations and I_{np} is defined as:

$$I_{np}(A,T_z) = B_n(A,T_z) + B_p(A,T_z) - B_{np}(A,T_z) \qquad (2\text{-}27)$$
$$B = \text{Binding energy}$$

The accuracy of this set of equations depends largely on how effectively I_{np} can be measured or calculated theoretically. For the tabulation of mass predictions edited by Maripuu (Ma 76g), Jänecke and Eynon use the most general solution to equations (2-26a) and (2-26b):

$$\Delta M(N,Z) = \Delta M_{eq} + H_1(N) + H_2(Z) + \eta_2\delta_{oo} + \eta_3\delta_{ee} + \eta_4\delta_{eo} + \eta_5\delta_{oe} \qquad (2\text{-}28)$$

where $\Delta M_{eq}(N,Z)$ is calculated from the binding-energy expression of Seeger and Howard (see section II-B3e). The symbols δ_{oo}, δ_{ee}, δ_{eo}, and δ_{oe} refer to odd-odd, even-even, even-odd, and odd-even nuclei, respectively. The binding energy expression of Seeger and Howard includes explicit dependences on both A and $T_z = T$; the mass predictions are determined using a χ^2-minimization procedure analogous to that of Garvey and Kelson. The final mass table is limited to nuclei with $A \geq 65$ because of the strong shell effects in light nuclei which are not properly calculated by the binding-energy expression.

c) Liran-Zeldes

The mass predictions of Liran and Zeldes are based on

the nuclear shell theory with the model coefficients determined from the known experimental masses (Ma 76d). More explicitly, the mass excess of a nucleus is written as:

$$\Delta M(N,Z) = N\Delta M_N + Z\Delta M_Z + (E_{pair}(N,Z) + E_{def}(N,Z) + E_{Coul})/c^2 \qquad (2\text{-}29)$$

where ΔM_N and ΔM_Z are the neutron and proton mass excesses, respectively. The first shell model term, $E_{pair}(N,Z)$, gives the ground state energy for a nucleus assuming strong pairing and isopairing (i.e., maximum number of $J_{12} = 0$ nucleon pairs and $T_{12} = 0$ neutron-proton pairs). E_{def} accounts for nuclear deformations resulting from one and two nucleon excitations to adjacent shells which leads to configuration mixing. These two terms are calculated differently for neutrons and protons filling the same shell and neutrons and protons filling different shells. E_{Coul} gives the Coulomb energy of the protons. In each term, the coefficients are first calculated separately for each major shell region (Ma 76d) and then readjusted over neighboring regions to insure continuity throughout the entire mass surface.

As described, the specification of the ground state configuration for an odd-odd nucleus is ambiguous. The experimental observation that nuclei in the $1f_{7/2}$ shell and above have $T_{gs} = T_Z$ except for N=Z nuclei which have

$T_{gs} = T_Z+1$ is used to remove the ambiguity (Ma 76d). In addition, the lack of Z>N experimental masses does not permit a least squares adjustment of the model coefficients for several shell regions. This difficulty is circumvented by using the parameters from the mirror nucleus, adding the properly renormalized Coulomb energy $E_{Coul.}$, from the $N \geq Z$ region, and requiring that all boundaries be continuous. Finally, the mass table excludes nuclei with 1p valence nucleons due to the improper treatment of the nuclear radius with changing A (Ma 76d).

d) **Groote-Hilf-Takahashi**

The macroscopic-microscopic model of Groote, Hilf, and Takahashi employs the Droplet model of Myers and Swiatecki and a modified level bunching techinque for the shell correction. The Droplet model is used both to calculate the macroscopic energy and to specify the free parameters of a Woods-Saxon potential which in turn specifies the location and the N,Z dependence of the magic gaps for the shell correction (Hi 75, Ma 76b). The use of the Woods-Saxon potential leads to the interesting anomaly of changing magicities with increasing deformation because the magic gaps depend on the l values of the gap defining single particle levels. Groote et al. speculate that the nucleons in high angular momentum orbitals get pushed out into the skin where few nucleons of the opposite kind reside, in nuclei far from stability, thus decreasing the number of

interacting partners. Four free parameters are needed per shell (two for protons and two for neutrons) to define the bunching strength and gap locations. For the mass predictions tabulated in (Ma 76b), Groote et al. use the deformation correction to the shell term of Myers and Swiatecki, but mention that use of a deformable Woods-Saxon potential could, in principle, incorporate nuclear deformation directly.

e) Seeger-Howard

Seeger and Howard begin with a modified liquid drop model and then use the Nilsson model to specify the wave functions used for calculating the shell correction and the odd-even pairing term (Se 75, Ma 76c). The liquid drop model, calculated in an ad hoc fashion, possesses many of the physical characteristics derived in a more unified fashion in the Droplet model. The shell correction is calculated using the deformed Nilsson orbitals and the Strutinsky normalization procedure. The ground state pairing energies are calculated using the Bardeen-Cooper-Schreiffer (BCS) formalism. Determination of all the free parameters except ε and ε_4, the quadrupole and hexadecapole Nilsson deformation parameters, is done by fitting the mass equation to the known ground state masses and fission barriers. The equation is then solved for all reasonable shapes ε and ε_4 to determine the maximum ground state binding energy.

f) Möller-Nix

The recent macroscopic-microscopic mass model of Möller and Nix (Kr 79, Mo 81b) is an offshoot of their work directed toward the calculation of fission barriers (Bo 72). A direct benefit of this effort is the ability of their mass model to calculate the ground state binding energy of highly deformed nuclei. Using the basic liquid drop model volume and volume asymmetry terms, and the Droplet model Coulomb terms, Möller and Nix add a surface term, calculated using a double Yukawa potential, to calculate the macroscopic energy (Kr 79). This double Yukawa potential is integrated over the desired nuclear shape to calculate the surface energy. Of note is the appearance of an A^0 term, which greatly improves the fit to the known mass data, and the lack of an $A^{1/3}$ term, introduced in the Droplet model. In addition, the neutron skin is ignored by letting $R_N = R_Z$. The microscopic term is composed of a shell contribution evaluated using the Strutinsky method and a pairing contribution evaluated using the BCS formalism (Kr 79, Mo 81b). The shell correction is evaluated in part by folding a Yukawa potential over a specified nuclear shape to obtain a diffuse spin-independent potential. This potential is added to a spin-dependent potential and a Coulomb potential to evaluate the total potential which is subsequently used for calculating the single particle energies.

The total binding energy is given in equation (2-30) along with a list of the free parameters. (Mo 81b).

$$
\begin{aligned}
E(Z,N,\text{shape}) = {} & M_H Z + M_N N - a_v(1-K_v I^2)A \qquad (2\text{-}30) \\
& + a_s(1-K_s I^2) I_n(r_o, a, A, \text{shape}) \\
& + E_{Coul.}(Z,A,r_o,\text{shape}) + E_{shell}(Z,N,\text{shape}) \\
& + E_{pair}(Z,N,\text{shape}) + E_{asymmetry}(W,I) + \Delta E
\end{aligned}
$$

r_o = nuclear radius constant a_s = surf. energy coeff.
a = range double Yukawa Pot. K_s = surf. asymmetry coeff.
a_v = volume coefficient w = asymmetry coeff.
K_v = volume asymmetry coeff. shape = shape dependence

The free parameters are determined from elastic electron scattering (r_o), heavy ion elastic scattering data (a), fission-barrier heights (a_s and K_s), and the known ground state masses (a_v, K_v, and W). Independently, specifying individual parameters avoids the problems often encountered when simultaneously determining all parameters through a χ^2-minimization procedure. Specific constants may be distorted during the minimization procedure because a physical effect requiring an additional term is missing. This procedure permitted the identification of several factors associated with the charge distribution of a finite sized proton, the charge diffuseness of the nucleus, the charge asymmetric part of the nuclear force and the microscopic zero-point energies, which should be included in the nuclear binding energy (Mo 81b). A measure of the

accuracy of this model is provided by the small change in the root mean square deviation of the binding energies (0.835 to 0.788 MeV) when a_s and K_s are allowed to vary during the fitting of equation (2-30) to the known ground state masses.

Table 2-2 lists the major attributes of the eight mass formulae just described. These models will be compared in section V to the known indium masses as an evaluation of their accuracy and to identify the systematic trends in the mass surface.

Table 2-2. Comparison of Selected Mass Formulae

Formula	Type	Number of Coeff.	Basis for formula	Characteristics
Garvey-Kelson (Jänecke)	mass relation	500	Garvey-Kelson transverse rel. + charge symmetric rel.	Set of homo. difference rel. fitted to known mass surface using χ^2-minimization.
Comay-Kelson	mass relation	100 mass skeletons	Garvey-Kelson transverse rel. + charge symmetric rel.	Localized determination of calculated masses. Surface avg. over different mass skeletons. Estimation of errors.
Jänecke-Eynon	mass rel. + macro-micro model	220	Generalized Garvey-Kelson relations	Inhomogeneous partial difference equations used to better cancel I_{np}, which is calc. using the Seeger macro. binding energy.
Liran-Zeldes	microscopic model	178	Semiempirical shell model calculation	Shell model calculation based on strong pairing and nonpairing. Inclusion of 1 & 2 nucleon excitations to adjacent shells. Parameters fitted to each shell region with continuity condition at boundaries.
Myers-Swiatecki	macro-micro model	16	Droplet model + shell calculation	Separate neutron-proton radii giving neutron skin. Second order expansion in $A^{-1/3}$. Linearly bunched Fermi levels for shell correction.
Groote-Hilf-Takahashi	macro-micro model	50	Droplet model + shell correction	Level bunching scheme using Woods-Saxon potential to calculate magic numbers and gaps for shell correction.
Seeger-Howard	macro-micro model	9	Modified LDM + shell corr. + BCS pairing energy	Nilsson orbitals used to calculate single particle energies for shell corr. and BCS pairing energy.
Möller-Nix	macro-micro model	9	Modified LDM + shell corr. + BCS pairing energy	Double Yukawa potential used to calculate macro. surface energy. Single Yukawa potential used to calculate potential defining single particle energies for shell correction and BCS pairing energy. Inclusion of A^0 term, proton form factor, exact charge diffuseness calc., nuclear charge asymmetry term and micro. zero-point E.

III. Experimental method

Examination of the $^{102-105}In$ beta decays employed an experimental procedure which may be summarized by the following four steps: 1) production of the indium isotopes, 2) mass separation of the isotope of interest, 3) observation of the subsequent β-decay, and 4) analysis of the resulting positron energy spectrum. More specifically, the isotope of interest was thermalized in 1.5 atm. of helium, after being produced by the interaction of the external beam from the Lawrence Berkeley Laboratory's 88-inch cyclotron with an appropriate target, and transported via a helium-jet to the ion source of the on-line mass separator, RAMA, where it was ionized, accelerated, and then mass separated. The resulting particle beam was collected on computer tape, creating a mass separated source, which was shuttled to a detection station for β-γ coincidence spectroscopy. The observed β-decays were analyzed event by event to create background subtracted energy histogram spectra, which were then corrected for the response characterstics of the β-detector, and finally replotted using the Fermi-Kurie representation to calculate β-endpoints. In the presentation below, each of the aforementioned steps will be discussed with special emphasis placed on those developments peculiar to these experiments (i.e., construction of the fast tape transport for shuttling radioactive samples collected on the RAMA focal plane to the detector station, design of a new scintillator based β-

telescope for electron (positron) energy measurements, and development of the computer analysis code for calculating β-endpoints from the measured energy spectra).

A) Production of isotopes

Figure 3-1 presents the experimental facilities of the spiral-ridge-focused, K=140 88-inch cyclotron (La 67). With the introduction of the Penning Ion Gauge (PIG) source, the cyclotron can routinely provide electrical microamperes of beams from protons to neon and, with less intensity, beams up to calcium. The maximum energy per nucleon varies from 50 MeV for $^{3}He^{+2}$ to 18 MeV for $^{14}N^{+5}$ and 13 MeV for $^{20}Ne^{+6}$. For the indium experiments, heavy ion beams of ^{12}C, ^{14}N, and ^{16}O were directed onto various targets to produce the isotopes of interest via (HI,xn) and (HI,pxn) reactions. More specifically, ^{102}In was produced via the $^{92}Mo(^{16}O,p5n)$ reaction at 125 MeV; ^{103}In was produced via the $^{92}Mo(^{14}N,3n)$ and $^{92}Mo(^{16}O,p4n)$ reactions with beam energies of 80 and 115 MeV, respectively; ^{104}In was produced using the $^{92}Mo(^{16}O,p3n)$ reaction at 95 MeV; and ^{105}In was produced via the $^{nat}Mo(^{14}N,xn)$ and $^{92}Mo(^{16}O,p2n)$ reactions with beam energies of 100 and 75 MeV, respectively. All targets were ∿2 mg/cm^2 thick; the average beam intensity varied between 2 and 4 eμA.

The target chamber of the RAMA separator is located in the cave 2 experimental beam line at the 88-inch cyclotron. The external particle beam is brought to a double focus just

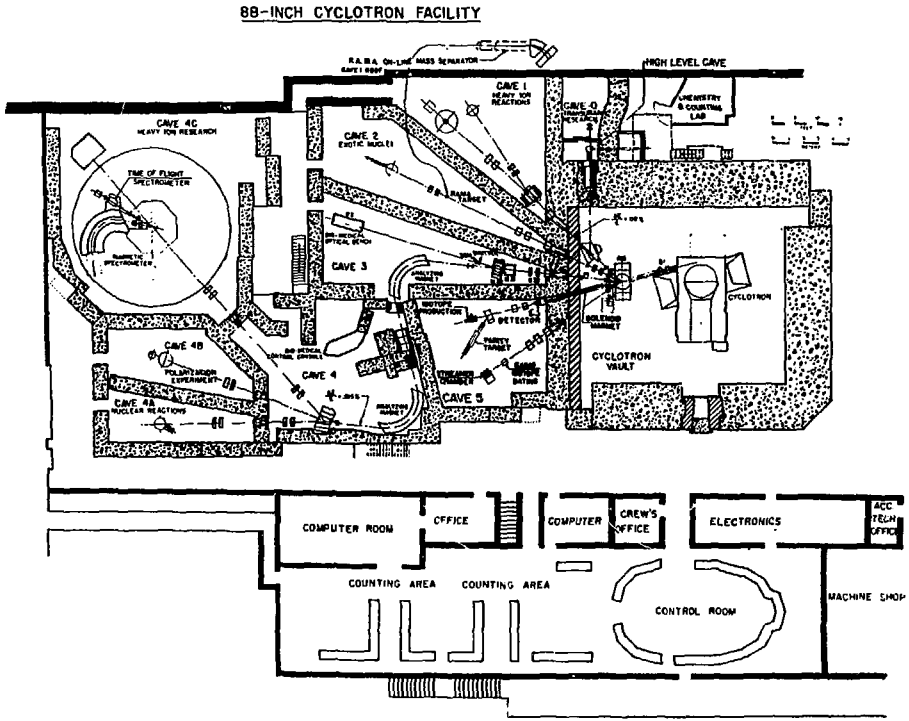

XBL 721-331F

Figure 3-1. Schematic of the 88-inch cyclotron facility. RAMA target chamber is located in the cave 2 beam line and connected to separator, positioned on cave 1 roof shielding, via a 6 m long helium-jet.

prior to entering the target chamber through the use of various quadrupole focusing and dipole bending magnets (see figure 3-1). Proper centering of the focused beam is monitored using a quartz reflector and circular collimator located immediately in front of the target chamber and a water-cooled Faraday cup located a few meters behind the chamber, which also measures the integrated beam. [Tests were conducted with a Faraday cup located at the rear of the target chamber to eliminate the exit foils (see section III-B1), but were discontinued due to the interference of the helium with accurate beam intensity measurements.]

B) Isolation of mass separated sources (RAMA)

For spectroscopy studies, the isotopes of interest must be isolated from the numerous recoils produced and "packaged" in a convenient form for observation by various detector arrangements. RAMA (see figure 3-2) accomplishes this task for β-decay studies by combining a helium-jet, a mass separator, and a fast tape transport.

1) Helium-jet

The helium-jet system has been used extensively (Ma 63, Se 73, Vi 78) for the efficient transport of radioactive nuclides away from high radiation background regions associated with accelerator beams. For the RAMA system, the helium-jet performs the traditional tasks of thermalizing and transporting the nuclear recoils, but must also accomodate to a further constraint requiring that the

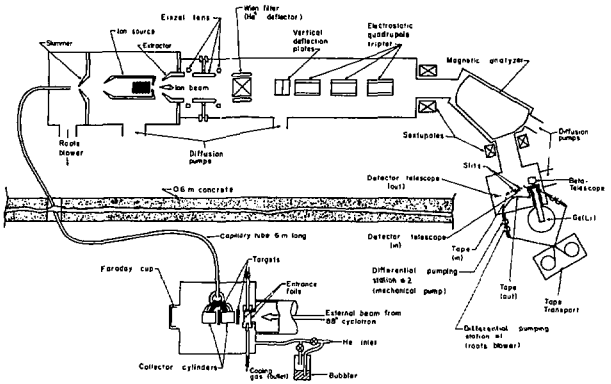

RAMA - 88 SCHEMATIC

XBB 810-11239A

Figure 3-2. Recoil Atom Mass Analyzer, RAMA. (top) Schematic of target chamber, helium-jet, separator and detector station. (bottom) View of RAMA with helium-jet entering from the left and the detector station located at the right. Large pump in foreground is a two stage Roots-blower for removing helium.

recoils exit from the capillary tube within a two degree cone (Go 72, Mo 79b, Mo 80a). This constraint originates from geometrical considerations associated with coupling the helium-jet to the plasma region of the RAMA ion source.

To understand as fully as possible those criteria which were included in the design of the RAMA helium-jet, a brief review of the operation of helium-jets is presented (Mo 79b). Essential to a helium-jet's efficient operation is the formation of large molecular weight clusters 10^3-10^8 amu to which the nuclear recoils attach themselves. Cluster formation is induced by the introduction of certain additives into the strongly ionizing radiation of the accelerator beam. Additives may be introduced by bubbling the helium through ethylene glycol, diffusion pump oil, acetone, or by passing the helium over sodium chloride heated to around 680°C. In addition, control of the helium gas temperature can be used to influence the size of the clusters. Other methods exist for achieving the same results, but will not be described here (Sc 75, Wo 76).

For the RAMA separator, a simple bubbler system using ethylene glycol as the additive has predominantly been used in conjunction with the accelerator beam and a temperature controlled target chamber to achieve efficient transport. The temperature at which the system is operated depends strongly on the character of the beam since heavy ions have a larger dE/dX than light ions and thus require a lower

operating temperature ($\sim 10^{o}C$) than the lighter ions ($\sim 20^{o}C$). Though the quantity of clusters produced is important, the size of the clusters, which is temperature sensitive, is even more stringent for efficient transportation because of the coupling of the helium-jet to the separator. Large clusters will exit the capillary tube with a smaller opening cone than smaller clusters. Experimentally, the transport efficiency, constrained by the 2° opening angle requirement, quickly approaches zero as the helium temperature is decreased below a certain minimum value. This efficiency gradually increases then decreases as the temperature is raised even though the overall helium-jet efficiency, measured by collecting all the activity exiting the capillary, continuously increases, which indicates the gradual transition from large to smaller clusters with increasing temperature.

Figure 3-3 shows the target chamber used with the helium-jet. Because the chamber is filled with helium, isolation foils are required to isolate the helium from the cyclotron vacuum. Double entrance and exit foil windows are used because of the need to cool the 2 mg/cm^2 thick Havar[1] foils (which are heated by the incident beam) by blowing cold nitrogen gas between the double foils The entire chamber is cooled using a Freon refrigerator coupled to two circular copper coils placed against the two outside walls which are perpendicular to the beam axis.

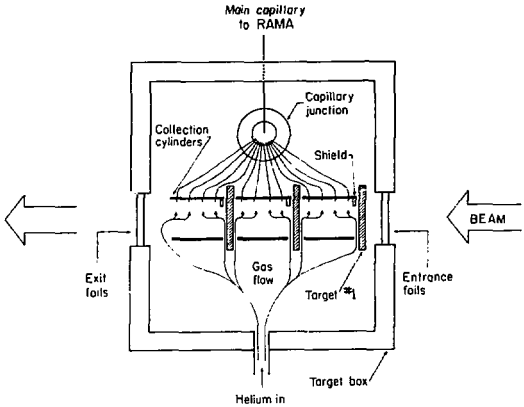

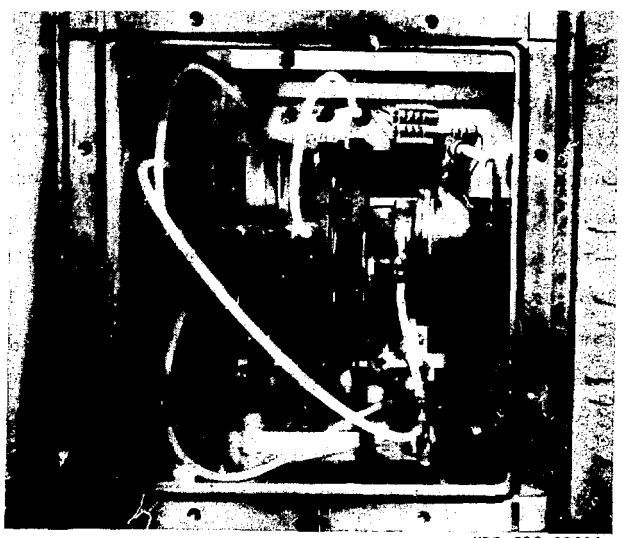

XBB 803-3383A

Figure 3-3. Helium-jet target chamber. (top) Schematic view of the target chamber with the three target system installed. (bottom) Inside view showing both isolation foil mounting fixtures and alternating target ladder-collection cylinder subsystem.

An obvious technique for increasing the overall yield of the helium-jet is to use multiple capillaries in each collection cylinder feeding into one large capillary as illustrated in the upper part of figure 3-3. Since the recoils travel only a limited distance in the helium, multiple targets must be used to insure that each capillary collects an approximately equal number of recoils. The optimum number of targets and capillaries depends on many factors including the recoil range, the energy drop of the beam per target, the added transport time from sweeping out a larger volume, etc. When using heavy ion beams, only two targets (each backed by six capillaries) can be used because of the large energy drop, per target, of the beams. (See appendix A for details). Even with this limitation, the overall yield increases about a factor of ten over that when using a single-target, single-capillary system.

The system using multiple capillaries feeds into a larger main capillary which then transports the recoils in the normal fashion. The multiple capillaries and the main capillary for these experiments were made from 1.0 mm i.d. (6.5 cm long) and 1.27 mm i.d. (6 m long) seamless stainless steel tubing[2], respectively. The helium flow rate, and thus the yield, varies as the capillary radius to the fourth power (Zi 74). However, experience shows that increasing the main capillary diameter much above 1.27 mm for our system produces a lower yield partly because of an increase

in the angle of the exit cone. Furthermore, large flow rates can disrupt the laminar flow [i.e., Reynolds number > 2000 (We 75)] essential to fast transport. (The Reynolds number is 570 for the 1.27 mm capillary with a helium flow rate of 2.5 liter/min. operating with a pressure differential of 1.5 atm and a temperature of ~10°C).

The lower view in figure 3-3 shows the inside of the target chamber with the multiple-capillary, multiple-target system installed. Each target is backed by a copper collection cylinder which is used for locating the multiple capillaries properly and for reducing helium turbulences near their inlets. The cylinders contain small semicircular collimators to prevent the cyclotron beam from striking the inlets to the capillaries which can also induce turbulence. The entire multiple-capillary, multiple-target system is mounted on a single plate for easy servicing. Opening of the chamber is minimized since the helium-jet then becomes severely disrupted and requires several hours to stabilize. This constraint led to the inclusion of externally moveable, three-position, target ladders.

The main capillary transports the activity produced in the target chamber to the RAMA separator where the recoils, which are attached to the large molecular weight clusters, are separated from the helium. The exit end of the capillary is directed at a flat skimmer with a 1.4 mm orifice which permits the clusters to pass to the ion source

chamber. Rapid expansion of the helium in the low pressure ($\sim$0.1 torr) skimmer chamber limits the helium leakage into the ion source region to that which escapes because of the pressure differential between the chambers (see figure 3-4). Both skimmer and helium-jet are moveable for centering on the RAMA beam axis. A large two stage Roots blower[3], capable of pumping 1500 l\s at a pressure of 0.1 torr, is used to remove the helium. Tests conducted using the β-delayed alphas from ^{20}Na [produced via the ^{3}He(^{24}Mg,α3n) reaction at 70 MeV] and the β-delayed protons from ^{111}Te [produced via the ^{12}C(^{102}Pd,3n) reaction at 80 MeV] indicate that approximately 20-70% of the activity exiting the capillary passes through the skimmer and approximately 40% of that is emitted within a 1° cone and 90% is emitted within the 2° cone necessary for entering the ion source. The angular distribution appears, thus, to include a narrow high density peak exiting at 0° with a fairly broad lower density tail extending out to large angles. In addition, the total transport time, t_d, (see appendix A) has been measured, using a pulsed cyclotron beam, to be 250-300 milliseconds.

2) Ion source and optics:

The ion source and related optical elements serve the purpose of producing a well focused beam which can be magnetically separated according to mass. The ion source used for these experiments is based on the Sidenius hollow-

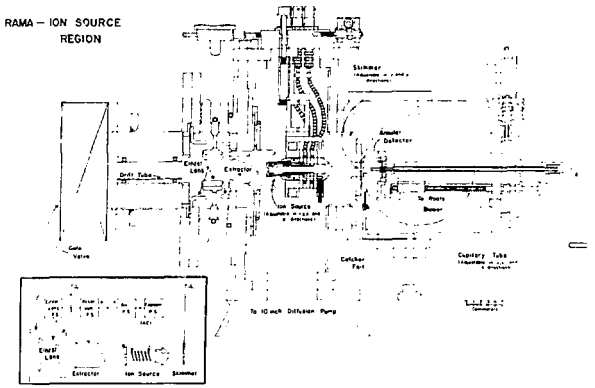

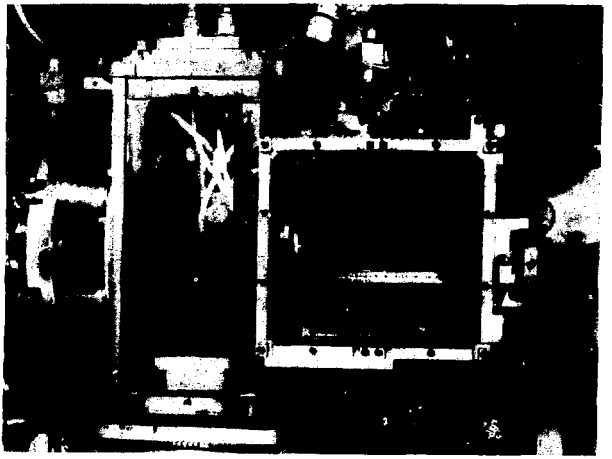

XBB 810-11247A

Figure 3-4. RAMA ion source region. (top) Schematic of helium-jet (directed at skimmer), ion source chamber, extractor, Einzel lens and drift tube. (inset) Electrical wiring schematic of ion source. (bottom) Photograph of helium-jet and ion source chambers.

cathode plasma source (Si 69). In this source, thermal electrons are emitted from a filament which is heated resistively. The electrons are accelerated by an electrical potential to about 200 volts which causes an externally supplied gas to be ionized, producing an arc and a positively charged plasma. (See inset top of figure 3-4). Ionization of the neutral nuclear recoils is postulated to occur predominantly by charge exchange with the ionized arc support gas (He^{+1}) and to a lesser extent by thermal ionization from the hot inner walls of the ion source.

The relative amount of ionization by these two methods depends on the melting point of the element of interest and on the operating temperature of the source. Group 1A elements used as calibration nuclei in these indium experiments [(K and Cs) see section III-D1] were ionized, in some tests, more efficiently with the arc discharge off (i.e., solely by thermal ionization) than with it on. The source operating temperature can be varied by changing the filament and arc operating conditions, and also by changing the materials from which the source is made. A detailed schematic of the source is presented at the top of figure 3-5. A unique feature of this source results from the use of an a.c. filament which eliminates the need for an external magnet to cancel the filament generated magnetic field. The source itself is approximately 9.0 cm long with an entrance hole 3 mm in diameter and an exit hole 1.6 mm in diameter;

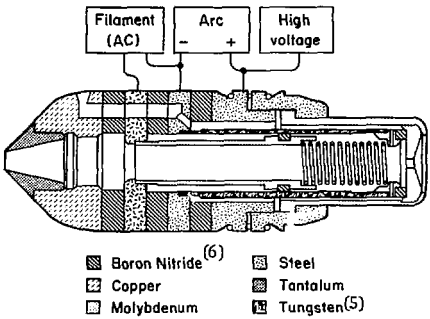

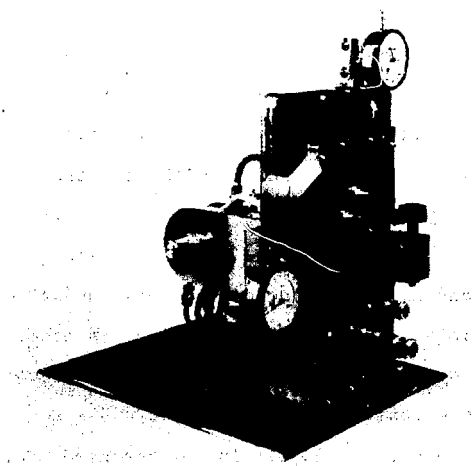

XBB 793-4156A

Figure 3-5. RAMA ion source. (top) Schematic of hollow-cathode ion source. (bottom) View of ion source in holder.

the entrance hole is located 3.6 cm from the skimmer. Typically, the source was run for the indium experiments as shown in figure 3-5 with a 6-turn, 25 mil tungsten[4] filament operating at 23 volts and 30 amps and an arc discharge operating at 250 volts and 1.7 amps. The operating temperature was estimated to be 1800-2000°C. The predominant limitation of this source is a low operating efficiency $\leq$0.5%. Advantages include its simplicity in design, a relatively long operating life ($\sim$24 hours) and ease in on-line servicing.

The source is held in position by molybdenum springs, which also serve as electrical contacts, contained inside a stainless steel, water cooled holder, which has quick disconnects for all external gas, water, and power connections (see bottom of figure 3-5.) Besides being easily removed and repositioned, this holder provides external (while inoperation) X, Y, and Z-positional adjustments. Mounting of the holder from above provides good vacuum pumping by the 10" diffusion pump immediately below it (see figure 3-4), eliminating almost all spark discharges caused by local outgassing. (Typical operating pressure is $2\text{-}4\times10^{-4}$ torr.) Since only the lower half of the holder and the ion source are floated at high voltage (18 kV), special aluminum oxide insulators and plastic water hoses insulate the system from ground. The water hoses presented an especially nettlesome difficulty because of the harsh

operating environment. Impolene tubing from Imperial Eastman[7] solved the problems (e.g. large scale flooding of RAMA) since it has good insulating properties and only melts above the boiling point of water.

Acceleration, focusing and mass separation of the beam is accomplished by a set of optical elements which includes, an extractor, an Einzel lens, a Wien filter, a set of vertical deflection plates, an electrostatic quadrupole triplet, two sextupoles, and a large dipole magnet. They were designed to achieve an overall mass resolution M/ΔM of 200 FW.1M. The extractor serves as the ground electrode which accelerates the ions out of the positively-biased source. A 3 mm diameter hole 1 cm from the ion source allows the accelerated ions to pass through the the extractor. Surrounding the extractor is a water cooled jacket which is required because of the proximity to the hot source. An Einzel lens located immediately downstream of the extractor serves to focus the beam and strongly influences the ultimate mass resolution obtainable. The Einzel lens consists of three circular electrodes: two ground electrodes which bracket a positively charged ring operating at between 10 and 16 kV depending on the alignment of the source. Following the Einzel lens is a 9 cm long, 2.2 cm diameter drift tube which serves as a space charge compensator. Stray helium ions scraping the sides of the tube eject electrons which join the central beam and reduce

space charge blow-up by reducing the beam's net positive charge.

Inclusion of a velocity or Wien filter is necessitated by the large He^{+1} beam (several hundred microamps) accelerated along with the nuclear recoils. Space charge considerations necessitate the removal of the helium before the beam enters the final focusing elements. The Wien filter consists of a vertical magnetic field and a horizontal electric field both oriented perpendicular to the central beam axis. Selection of the magnetic and electric field strengths is determined by a) the deflection of the helium beam by 4° to 12° and b) the undeflected transmission of the mass ($\pm$10%) of interest. The next two optical elements are a set of electrostatic deflection plates and a quadrupole triplet which serve to center vertically and then focus the beam for proper acceptance by the dipole bending magnet. An electrostatic quadrupole (with the first and third elements connected together) is used for its mass independent characteristics.

Mass separation of the beam is performed by a surplus beam bending magnet originally employed for the deflection of the external cyclotron beam. Use of this magnet necessitated the design of a 75.5^{o} separator and the inclusion of field clamps and two sextupoles which correct for second order aberrations. Tests using internally generated beams measured the final resolution ($M/\Delta M$) of the

separator at close to 200, with a dispersion of 1.64 m. For an extended description of the RAMA separator consult (Mo 79b, Mo 80a, Mo 80b, Mo 81a).

3) Detector chamber and tape transport:

Design of the detector chamber centered on creating a system with maximum versatility and ease of use (See figure 3-6). The chamber consists of multi-ported master flanges for the top and three sides which permit the convenient mounting of instrumentation. A six inch diffusion pump serves to evacuate the $(0.5x0.5x0.3)m^3$ chamber to $1x10^{-6}$ torr. The versatility of this design greatly facilitated the addition of the tape transport for large volume detectors and currently supports an extensive variety of detector arrangements.

A set of variable size slits (0-2 cm opening) is located at the center of the detector chamber and defines the position of the focal plane. Detectors or the tape transport are positioned directly behind these slits for collection of mass separated samples. A channel electron multiplier (CEM) [see (La 81) for principle of operation], fixed to a moveable slide, can be positioned directly behind the slits. This CEM is connected to a Faraday cup and is used for calibrating the separator and focusing the beam. Internal beams of $^{20}Ne^{+1}$, $^{40}Ar^{+1}$, etc. may be generated, by introducing the appropriate impurity gas in the arc support gas, for calibrating at various masses. For the indium

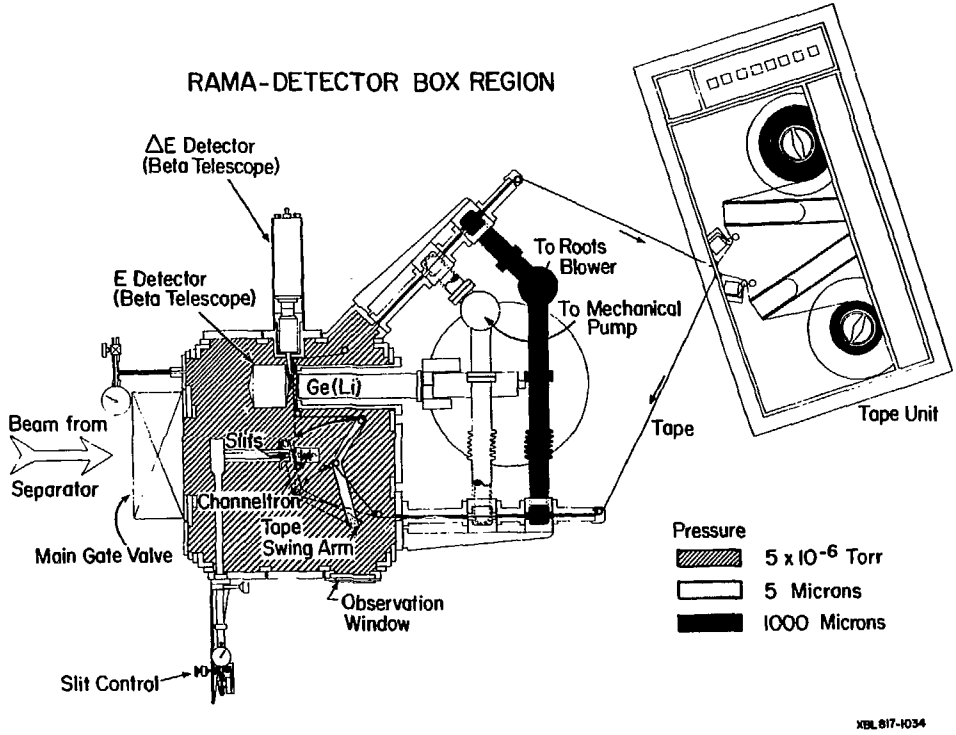

Figure 3-6. *RAMA detector box region. Schematic of detector chamber with tape transport and β-γ detector station included.*

experiments, molybdenum isotopes evaporated from the inner walls of the ion source and tin isotopes introduced as tetraethyl tin (Mo 79b) in the arc support gas served to calibrate the separator. For mass 100, the spacing between adjacent masses is 8.0 mm and the slit opening used is 3.5 mm which results in less than a 0.1% contamination from the neighboring masses.

The $\beta-\gamma$ coincidence measurements of interest between large volume detectors, necessitated the development of a shuttle system to collect mass separated sources and position them accurately between the detectors. Availability of a used Datamec computer tape drive resulted in the the differentially pumped tape transport illustrated in figure 3-6. Advantages in using a commercial unit include high positional accuracy ($\sim$2 mm), fast transport speed (125 ms transport time to $\beta-\gamma$ detector station) and proven reliability. The obvious disadvantage is the necessity of building two differentially pumped arms that pass the tape in and out of the detector chamber. These arms each consist of two pumping stations and three isolation channels which bring the pressure from an atmosphere in several stages: 1 torr first station; 5×10^{-3} torr second station; to 5×10^{-6} torr in the detector chamber. The first stage is pumped by a single stage Roots blower[3] capable of pumping 650 l/s of air while the second stage is pumped by a mechanical pump capable of pumping

10 l/s of air. Chrome-plated brass slits 1.7 cm tall, 7.6×10^{-3} cm wide (3 mils) and 2.0 cm deep are located at the entrance and exit of each isolation channel to impede the flow of air. Each arm was pinned, after centering the individual parts with a mandrel, to prevent the tape from being snagged by the slits. Low inertia, Lucite rollers on ball bearings[8] guide and center the tape as it moves through the system. Periodic calibrating of RAMA required the installation of a pivoting tape support guide inside the detector chamber which pulls the tape back from the slits to allow proper positioning of the CEM.

Numerous advantages are associated with using a tape transport over other systems, especially for β-decay spectroscopy. Direct collection of the mass separated beam yields thin sources which eliminates problems with self-absorption. Careful selection of the tape cycling period can enhance the yield of the activity of interest versus activities with different half-lives (see appendix B). Lastly, cycling of the tape reduces background from long-lived daughter nuclei.

C) Detection system

For β-γ coincidence experiments the detector station consists of a scintillator telescope, positioned facing the source side of the tape, for β counting and a 15% coaxial Ge(Li) detector, located on the opposite side of the tape, for γ counting (see figure 3-6). Both detectors are

extensively shielded by lead bricks to reduce the neutron background from the cyclotron beam and the Ge(Li) detector has an additional copper shield to reduce the Compton background. Figure 3-7 presents an interior view of the detector chamber looking directly at the slits with the β-telescope at the right.

The β-telescope designed to stop up to 20 MeV electrons consists of a 10 mm diameter and 1 mm thick NE102 plastic scintillator as a ΔE counter (for γ-ray rejection) and a large cylindrical NE102 plastic scintillator, 11.4 cm in both diameter and length, as an E detector. The E counter is tapered to reduce the inactive volume. To achieve a high β-detection geometry (24%), the detectors are positioned within 3 mm of each other and the ΔE is located approximately 3 mm from the source, deposited on the tape.

Each detector includes, along with the scintillator, a light pipe and a photomultiplier (pm) tube. The scintillator and lightpipe (Lucite) are individually machined and polished, then glued together and covered with 2000 angstroms of evaporated aluminum. Black paint is sprayed over the entire assembly, except the entrance windows (and exit window of the ΔE) for light tightness. The lightpipe is joined optically to the pm tube using Q2-3067 optical coupling grease[9]. Two different pm tubes are used: an RCA 8850 for the ΔE and an RCA 8575 for the E[10]. The 8850 has a gallium-phosphide first dynode with a gain of 40 which is

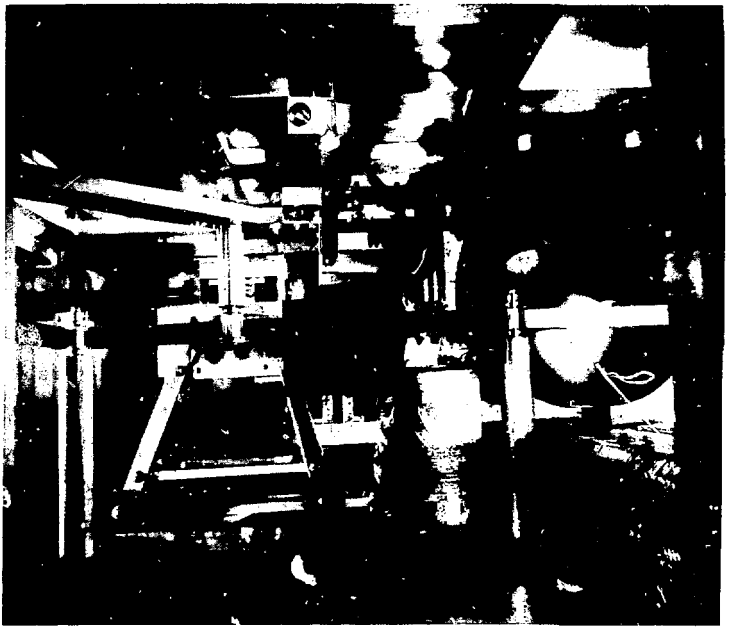

XBB 810-11245

Figure 3-7. Photograph looking directly at slits defining the focal plane of the detector chamber. Moveable tape guide enters picture from top left, CEM is small spiral tube at top center and β-telescope is at right center. Ge(Li) detector is removed for photograph.

necessary to amplify the small signals emanating from the ΔE detector, while the 8575 has a standard copper-beryllium first dynode with a gain of 6 which is also used for all the remaining dynodes in the two pm tubes. Both pm tubes employ twelve dynode amplification stages and are typically biased at -2300 volts. The lightpipe and scintillator are also biased at -2300 volts to reduce the stray electric field near the pm tube and thus reduce the dark current. To further reduce this current, the pm tube is wrapped in several shields, beginning with a layer of white reflective tape and a layer of black photographic tape applied to reflect internally emitted light into the pm tube and to eliminate external light leakage. These layers are surrounded by a 1 mil layer of conductive tape which is biased at the pm tube bias voltage. Two 5 mil Mylar layers are then applied for insulation. Four 5 mil layers of grain oriented steel, for magnetic field suppression, are added in succession with each layer rotated 90° to the previous layer. Finally, the entire assembly is surrounded by black tape, which protects the inner layers.

The Ge(Li) detector employed is an Ortec[11] WIN[15] series with a nominal resolution of 2.3 keV at 1332 keV. Since the detector had previously sustained appreciable neutron damage, the resolution was only 8-10 keV at 1332 keV for the indium experiments. The crystal is positioned within 1 cm of the tape resulting in a solid geometry of

$\sim$30% and is isolated from the vacuum of the detector chamber by a 2.54×10^{-3} cm (1 mil) thick aluminum window. For $\beta - \gamma$ coincidence experiments the overall solid geometry is $\sim$7%.

Standard fast-slow coincidence networks are employed using the three detectors so that both singles spectra as well as β-γ coincidence spectra can be obtained (see figure 3-8). The final coincidence timing of 5 ns (FWHM) between the two scintillators and 20 ns (FWHM) between the β-E scintillator and the Ge(Li) counter (see figure 3-9) greatly reduces chance coincidences between detectors because of the modest maximum singles counting rate (<2000 counts/second) in each detector. The slow rise time of the Ge(Li) signal compared to that of the β-E detector causes the increased FWHM for the $\beta - \gamma$ TAC and also is responsible for the pronounced tail, which is strongly dependent on the termination of the time signal cable out of the Ge(Li) preamplifier. (Fast signals for the two scintillators are picked up from the respective anodes.) Pile-up rejectors are used for all three detectors primarily because the various timing and coincidence requirements are set up using very hot calibration sources. All electronics are blanked out by a master gate generator while the tape transport, which is controlled by a master clock, is cycling. The master gate generator also resets and starts, after each tape cycle, the clock of a multiple event TAC which labels each event with a time of occurence for half-life

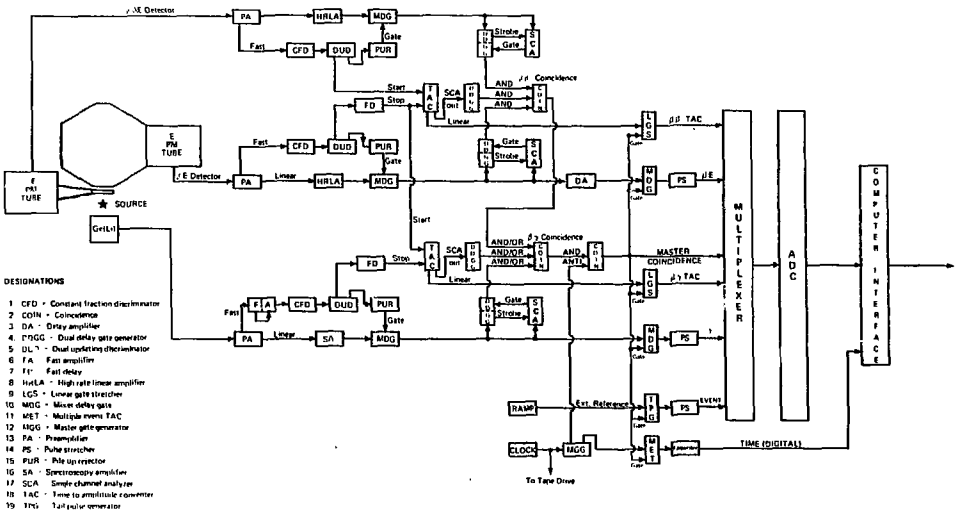

Figure 3-8. Schematic of electronic set-up used with β-telescope and Ge(Li) detector for β-γ coincidence experiments.

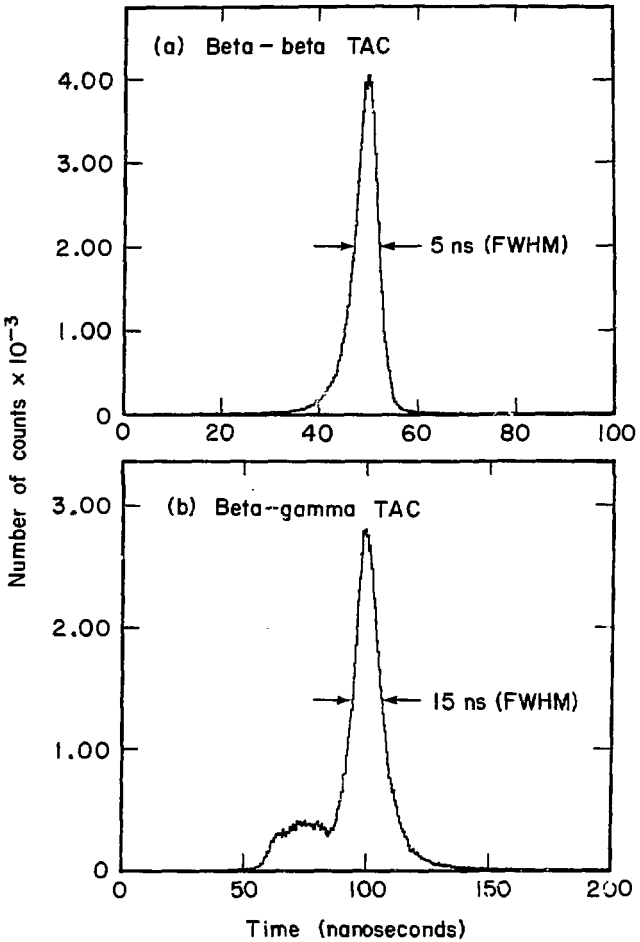

XBL8111-1641

Figure 3-9. a) β-β TAC and b) β-γ TAC spectra. Inherently poorer timing signal from Ge(Li) detector relative to photomultiplier tubes of β-telescope result in larger FWHM in β-γ TAC spectrum.

determinations. A novel unit developed especially for RAMA sends out a signal, proportional to the height of a ramp, for every event recorded. This ramp increases in height linearly with time so that a measure of the number of counts in a given unit of time (∿8 minutes) is obtained which permits the continuous monitoring of the RAMA yield.

Six parameters are thus recorded for each observed decay: event, β-energy, γ-energy, β-β TAC, β-γ TAC, and time. The first five proceed through a multiplexer-ADC system and are stored on magnetic tape as multiparameter event data using the **CHAOS** [now called **MINUS3** (Ma 79)] acquisition and analysis FORTRAN code running on a Modcomp IV/25 or Classic computer[12]. The sixth parameter, time, is added directly as a digital word to the data stream by a tagwriter.

Typical operating conditions resulted in a β-γ coincidence counting rate which varied from ∿20 counts/minute for ^{38}K and ^{66}Ga to ∿50 counts/minute for ^{62}Cu and the two Cs calibration nuclei. Indium counting rates were substantially lower with ∿2 counts/minute for ^{103}In up to 15 counts/minute for ^{105}In. β-singles counting rates were a factor of twenty higher than β-γ coincidence rates. 6000 coincidence events with a minimum kinetic energy of ∿1 MeV constituted an average β-spectrum.

D) Analysis of data

1) β-endpoint determination

Analysis of the observed β-spectra to obtain the final β-endpoints is accomplished via a three step procedure which includes: 1) removal of beta background, 2) correction for response function of beta E detector, and 3) plotting of data in Fermi-Kurie form in order to calculate a weighted linear least-squares fit. Step 1, beta background subtraction, begins by generating histogram spectra event by event, using **CHAOS** with coincidence gates set on the β - β and β-γ TACs and, in the appropriate cases, on the 511 keV annhilation peak or on the gamma line resulting from a known transition in the daughter nucleus. Most of the spectra are each corrected for background by subtracting the corresponding histogram spectrum generated by reanalyzing the event data using identical TAC gates, but including now, a gamma gate immediately above and of the same width as the original gate used. For those selected spectra gated just by the two TACs, no background subtraction is needed since the spectra are obtained with high counting rates over a brief time interval, and inclusion of a gamma gate does not remove ambiguities resulting from multiple beta branches to the daughter. (Compare decay schemes of ^{104}In, figure 4-4, and ^{105}In, figure 4-5.) Only the ^{104}In data were deemed suitable for exclusion of the background correction and even these were analyzed using both techniques. Summaries of the

gamma gates employed are included in tables 3-1 and 4-2.

Several physical processes must be considered in determining the response function of a scintillation based telescope to positrons (electrons) including backscattering of positrons (electrons) out of the detector, summing of the positron annihilation and kinetic energies (pile-up), and the finite energy-resolution of the detector (Be 69a, Wo 72). Concern over an additional effect, that due to gamma background radiation, is precluded by using a telescope with the ΔE scintillator serving as a γ-ray reject detector. Backscattering affects, predominantly, the low energy portion of the observed β-spectrum by including an excess number of low energy signals resulting from the incomplete energy loss of the positron (electron) in the detector. For β-endpoint determinations above a few MeV, this effect may be minimized by excluding the low energy portion of the β-spectrum from the endpoint analysis. Pile-up effects have been measured explicitly by Beck (Be 69a) and were shown to cause only small distortions near the β-endpoint for an E scintillator similar to the one employed in these experiments. Furthermore, the pile-up effect is easily observed in the Fermi-Kurie plots as a deviation near the endpoint from the expected linear behavior, and thus that portion of the plot may be excluded from the least-squares analysis. Further, employment of positron emitters as calibration standards limits any systematic deviation

which might result from pile-up effects.

The predominant effect governing the response function of the scintillation detector is its finite energy resolution, which results from the limited number of photons generated by each detected positron (electron). These limited statistics result in an approximately Gaussian response by the detector to a beam of monoenergetic electrons with a FWHM that varies as the $\sqrt{E}$ (Be 69a, Ot 79). However, the measured energy linearly follows, to high accuracy, the electron beam energy from 1 MeV to well over 20 MeV (Be 69a, Ne 74, Ot 79). These considerations lead to the use of a Gaussian response function with a $\sqrt{E}$ dependence for the FWHM which was determined to be 200 keV at 976 keV by using the conversion electrons from ^{207}Bi.

$$R(E,E') = (\sigma_1\sqrt{2\pi E'})^{-1}\exp\{-(E-E')^2/2\sigma_1^2E'\} \quad (3\text{-}1)$$

$$\sigma_1 = 0.426 \times \text{FWHM at 1 MeV}$$

$$\int_0^\infty R(E,E')dE = 1$$

The correction for the finite energy resolution of the E scintillator is calculated by using the theoretical shape, T(E), (see equation 2-11) for the beta spectrum with endpoint energy W_o (E_o) and distorting it using the semi-empirically derived response function, R(E,E'), for the E detector. This procedure, initially suggested by Rogers and Gordon (Ro 65), yields an energy dependent factor, K(E), by which the measured beta spectrum, O(E), is multiplied to

obtain the undistorted beta spectrum, N(E).

$$M(E) = \int_0^\infty T(E')R(E,E')dE' \qquad (3\text{-}2a)$$
$$K(E) = T(E)/M(E) \qquad (3\text{-}2b)$$
$$N(E) = K(E) \times O(E) \qquad (3\text{-}2c)$$

The final endpoint is calculated by graphing the beta spectrum in Fermi-Kurie form (Ku 36) and least squares fitting a straight line to the resulting plot. Proper weighting of the fit is determined by:

$$w_i = 1/\sigma_i^2 \qquad (3\text{-}3)$$

(not to be confused with σ_1) where

$$\sigma_i^2 = \sigma_{N_i}^2 (dY_i/dN_i)^2 + \sigma_{F_i}^2 (dY_i/dF_i)^2 \qquad (3\text{-}4a)$$
$$Y_i = (N_i/F_i p_i W_i)^{1/2} \qquad (3\text{-}4b)$$

In equation (3-4a) N_i is the number of counts in channel i and F_i is the corresponding Fermi function (see section II-A2). Y_i is just the function defined in equation (2-8) which is plotted versus W_i to obtain the Fermi-Kurie representation. Since F_i varies quite slowly with energy and can be accurately calculated, the second term in equation (3-4a) may be set to zero. With σ_{N_i}, the error in the number of counts, N_i, in channel i, equal to $\sqrt{N_i}$, w_i just becomes:

$$w_i = 4p_iF_iW_i \qquad (3\text{-}5)$$

Since W_o is initially estimated the outlined procedure must be repeated until the estimated W_o agrees with the calculated W_o. The iteration converges very rapidly and gives almost the exact endpoint with the first iteration if the initial estimate is within approximately 400 keV of the actual value of W_o. Furthermore, the linearity of the Fermi-Kurie plot improves with more accurate estimates of W_o. Figure 3-10 illustrates the effect of including the detector response function correction [see N(E) curve] as opposed to leaving it out [see O(E) curve] for a theoretically generated spectrum with a 3.5 MeV endpoint. The effect is especially noticeable for multiple branch decays when only the upper portion of the Fermi-Kurie plot can be used for the endpoint analysis. Figure 3-11 summarizes the procedure for determining a beta endpoint.

Analysis of an unknown endpoint begins with determining the energy calibration. Each "standard" nucleus is analyzed using the above procedure to determine the channel associated with a given energy, and several iterations are required to specify the calibration. The quality of the calculated calibration, so determined, can be judged by the linearity of the Fermi-Kurie plots as well as by the χ^2 resulting from the linear least-squares fit to the calibration nuclei (literature energy versus channel

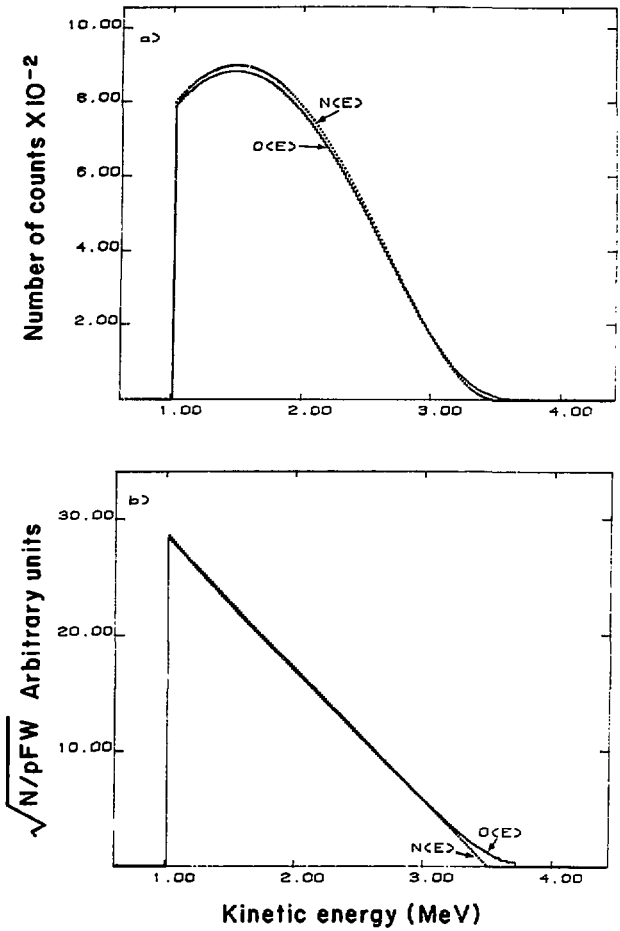

XBL 8111-1615

Figure 3-10. a) Observed, O(E), and detector response corrected, N(E), theoretical β-spectra. b) Fermi-Kurie plots of detector response corrected, N(E), and not corrected, O(E), β-spectra.

CORRECTION FOR DETECTOR RESPONSE

GIVEN: Response function (semiempirical):

$$R(E,E') = (\sigma(E')\sqrt{2\pi})^{-1} * \exp\{-(E-E')^2/2\sigma(E')^2\}$$

$$\int R(E,E')dE = 1$$

experimentally observed that: $\sigma(E') = \sigma_1 * E'$

PROCEDURE:

1) **Use theoretical beta spectrum, T(E), and estimated E_o to calculate distorted spectrum:**

$$M(E) = \int_0^\infty R(E,E')T(E')dE'$$

2) **Calculate correction factor to O(E):**

$$O(E)/N(E) = M(E)/T(E) = 1/K(E)$$

O(E) = observed spectrum
N(E) = positron spectrum

3) **Calculate N(E):**

$$N(E) = K(E)*O(E)$$

4) **Plot in Fermi-Kurie form:**

$$N(E)/\{G(E)*(E+0.511)^2\} \text{ vs } E$$

G(E) = modified Fermi function.

5) **Perform linear least squares fit:**

Determine E_o. Use this new E_o in T(E) and repeat steps 1-5 till E_o stabilizes.

Figure 3-11. Procedure for determining β-endpoint energies from background-subtracted histogram spectra

number). A serious deviation from the correct intercept would affect the Fermi-Kurie plots by either making them concave, if the intercept were too large, or convex, if the intercept was too small. Figure 3-12a presents the Fermi-Kurie plot from the decay of ^{38}K, one of the calibration nuclei, with the appropriate error bars as an example of the weighted linear least-squares fits obtained. Figure 3-12b presents the overall calibration as determined using the calibration activities (Le 78, Ep 79) listed in Table 3-1; a good linear fit was obtained. Table 3-1 also presents for each calibration activity the γ-gate employed to obtain the β-spectrum and the reaction used for its production. Figure 3-13 presents the partial decay schemes of the calibration nuclei indicating the predominant β-branches and the known spins and parities of the major levels.

2) Error analysis:

A two step procedure is used for calculating the error in the individual endpoints. A statistical error is determined using the formalism of Rehfield (Re 78) which weights the Fermi-Kurie plot by the factor given in equation (3-5) and determines the error in the endpoint to be (see appendix C)

$$\sigma_{W_o}{}^2 = (1/A^2\Delta) \sum_i (W_o - W_i)^2/\sigma_i{}^2 \qquad (3\text{-}6a)$$

where

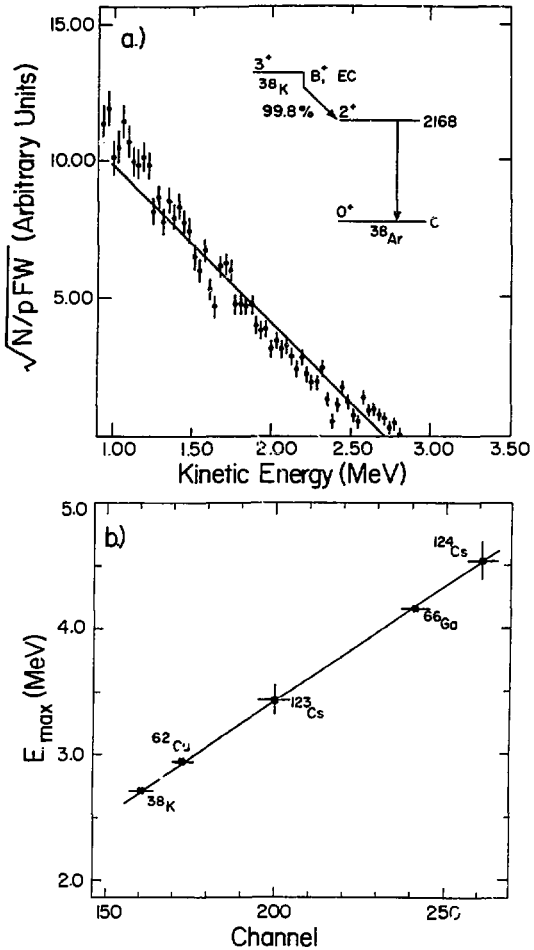

Figure 3-12. a) Fermi-Kurie plot of the ^{38}K positron spectrum in coincidence with the 2168 keV γ transition in the daughter. b) Energy calibration for the β-telescope using the calibration activities listed in table 3-1.

Table 3-1. Calibration Nuclei

Nuclide	Half-life	Gate (keV)	E_{max} (MeV)	Reaction
^{38}K	7.6 min.	2168	2.724±0.002	$^{24}Mg(^{16}O,pn)$
^{64}Cu	9.7 min.	511	2.927±0.005	$^{52}Cr(^{12}C,pn)$
^{123}Cs	5.9 min.	97	3.410±0.122	$^{nat}Cd(^{14}N,xn)$
^{66}Ga	9.4 hr	511	4.153±0.004	$^{52}Cr(^{16}O,pn)$
^{124}Cs	31.0 sec.	354	4.573±0.150	$^{nat}Cd(^{14}N,xn)$

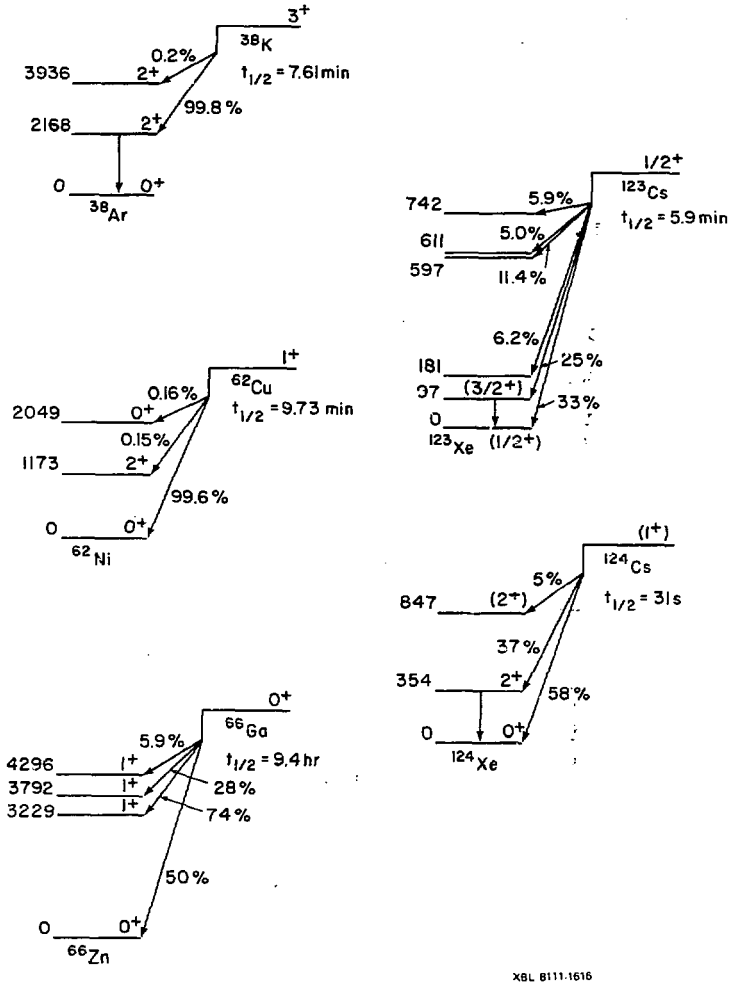

Figure 3-13. Partial decay schemes of calibration nuclei: ^{38}K, ^{62}Cu, ^{66}Ga, ^{123}Cs and ^{124}Cs. 511 keV γ's or, where indicated by arrows, first excited state to ground state transitions in the daughters were used for gating β-spectra.

$$\Delta = \sum_i (1/\sigma_i^2) \sum_i (W_i^2/\sigma_i^2) - [\sum_i (W_i/\sigma_i^2)]^2 \qquad (3\text{-}6b)$$

In these expressions A is the slope of the Fermi-Kurie plot, F_i is the Fermi function, and W_o is the endpoint energy; the energy corresponding to channel i, W_i, is summed over the energy limits of the least-squares fit. This error, σ_{W_o} which accounts only for the energy range and the number of counts included in the fit, must be adjusted to include the error associated with the goodness of the fit. Variation of the energy limits governing the least-squares fit and requiring a reasonable χ^2 for each fit provides a measurement of the possible variation in the endpoint energy for a given Fermi-Kurie plot. Inclusion of these two sources of error specifies the total error in determining the x-intercept of a Fermi-Kurie plot, σ_{FK}, and is the only experimental error associated with the calibration nuclei. This error along with the literature endpoint energies and errors, and the corresponding channel numbers and errors, is used to obtain the error due to the energy calibration of the β-telescope (see appendix C)

$$\sigma_{W(calib)}^2 = \sum_i^N \{\sigma_{lit}^2 [X_o(df_A/dW_i) + (df_B/dW_i)]^2 + \sigma_{FK}^2 [X_o(df_A/dX_i) + (df_B/dX_i)]^2\} \qquad (3\text{-}7)$$

$$f_A = f_A(W_i, X_i)$$

$$f_B = f_B(W_i, X_i)$$

In equation (3-7) the slope f_A and the intercept f_B of the calibration function depend on the literature values for the endpoints of the calibration nuclei W_i with uncertainties σ_{Lit_i} and the corresponding measured channel numbers X_i with error σ_{FK_i}. The channel number corresponding to the calculated endpoint energy W_o is indicated by X_o and N is the number of calibration nuclei. Quadratic addition of the energy calibration error with σ_{FK} provides the total error associated with an unknown endpoint determination.

All endpoints determined for the indium experiments were calculated by the FORTRAN computer code SPECTR (Wo 81a) which can be run on a ModComp IV/25 or Classic computer[12]. This code calculates the detector response correction, plots the data in Fermi-Kurie form, performs the weighted linear least-squares fit, determines the energy calibration and calculates the individual errors. In addition, all final spectra were plotted using SPECTR and a Textronix 4662 flat bed plotter.

IV Results

The final results for the indium experiments are presented in table 4-1 which lists the γ-lines and their relative intensities observed following the β-decay of ^{102}In and ^{103}In, and table 4-2, which lists the calculated Q_{EC}'s of $^{103-105}$In (see also Wo 82). Figure 4-1, which presents the γ-spectrum observed at mass 102 for isotopes produced with a 125 MeV ^{16}O beam incident on an 80% enriched ^{92}Mo target, reveals the presence of two new γ-lines of approximately equal intensity at 777 and 852 keV, which decay with a 20±5 sec. half-life. Observation of these two lines confirms the identification of ^{102}In by Béraud et al. (Be 81a, Be 81b) who also observed two γ-lines at 396.5 keV and 593.0 keV decaying with a half-life, which they determined to be 24±4 sec. The tentative decay scheme presented in figure 4-1, which was determined by both in beam (Tr 81) and decay experiments (Be 81b), shows the distinct ground state band 0^+, 2^+, 4^+... present in the heavier even-even cadmium daughters.

Close examination of the γ-spectrum of ^{103}In (see figure 4-2a) in coincidence with β's revealed two γ-rays at 720 and 740 keV, decaying with the proper half-life of 60.5 sec, along with the 188 and 202 keV γ-rays observed previously by Lhersonneau et al. (Lh 78). The observation of these γ-rays is in agreement with the recent results of Béraud et al. (Be 81a), although the relative intensities of 32 and 19%, which are quoted for the 720 and 740 keV γ-rays,

Table 4-1. Relative Intensities of the γ-Rays in the Decay of ^{102}In and ^{103}In

^{102}In		^{103}In	
E (keV)	I	E (keV)	I
777	∿100	188	100
862	∿100	202	16±3
		720	18±3
		740	13±2

Table 4-2. Summary of the Q_{EC} Determinations

Nuclide	Gate(s)	E_{MAX} (MeV)	Q_{EC} (MeV) This Work	Q_{EC} (MeV) Literature
^{103}In	188	4.17±0.13	5.38±0.13	5.8±0.5 (Lh 78)
^{104}In	658,834 NO GATE	4.91±0.14	7.42±0.14	7.42±0.2 (Hu 78)
^{105}In	131	3.99±0.13	5.14±0.13	-------

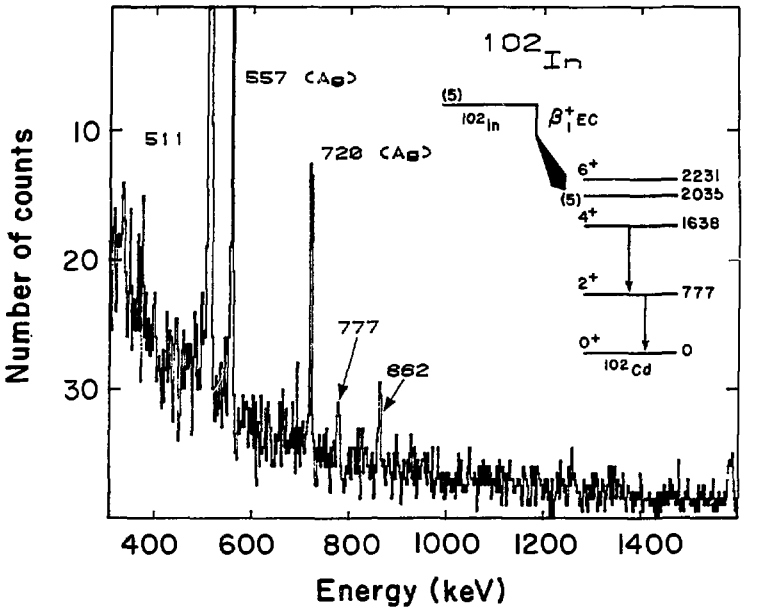

XBL 8111-1614

Figure 4-1. Mass 102 γ-spectrum with ^{102}In transitions indicated by arrows. Partial decay scheme is from Béraud et al. (Be 81a).

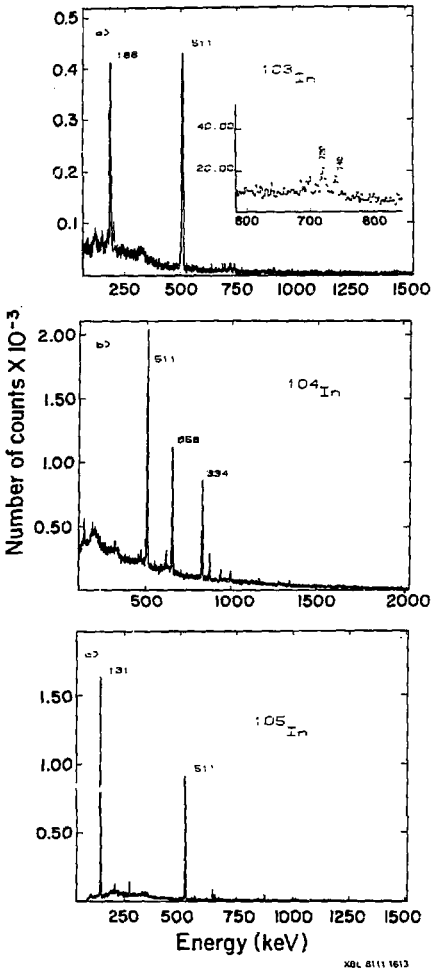

Figure 4-2. γ-spectra observed for a) ^{103}In, b) ^{104}In and c) ^{105}In. Inset, figu e (a), shows two new lines observed at 720 and 740 keV for ^{103}In.

respectively, are slightly higher than our results indicate. Based on the reaction work of Meyer et al. (Me 80), the 720 keV γ-ray corresponds to the first member of a decoupled band based on the 188.1 keV $7/2^+$ state.

The Fermi-Kurie analysis of the positron spectrum from ^{103}In in coincidence with the 188 keV γ-transition in the ^{103}Cd daughter is shown in figure 4-3. A partial decay scheme is also given in this figure for ^{103}In with the beta branching ratios determined from the measured relative γ-intensities. Figure 4-3 shows that the linearity of the Fermi-Kurie plot is not affected seriously by the small β-feeding of the $11/2^+$ level.

Figures 4-4 and 4-2b present, respectively, the Fermi-Kurie analysis for the ^{104}In positron singles spectrum together with a partial decay scheme and the γ spectrum in coincidence with the positrons. The decay scheme of ^{104}In has been studied intensively by Huang et al. (Hu 78). According to their work, about 22% of the beta decay goes to the second excited state (4^+) at 1492 keV, while the first excited state (2^+) at 658 keV is not fed directly. All the higher lying levels deexcite to the 4^+ level by γ-ray emission. Since approximately 50% of the β-decay strength feeds three close-lying states at 2370.2, 2435.4, and 2492.3 keV, the energy range for the least-squares fit to the data in the Fermi-Kurie plot is restricted to the highest 1 MeV of the data. Positron spectra in coincidence

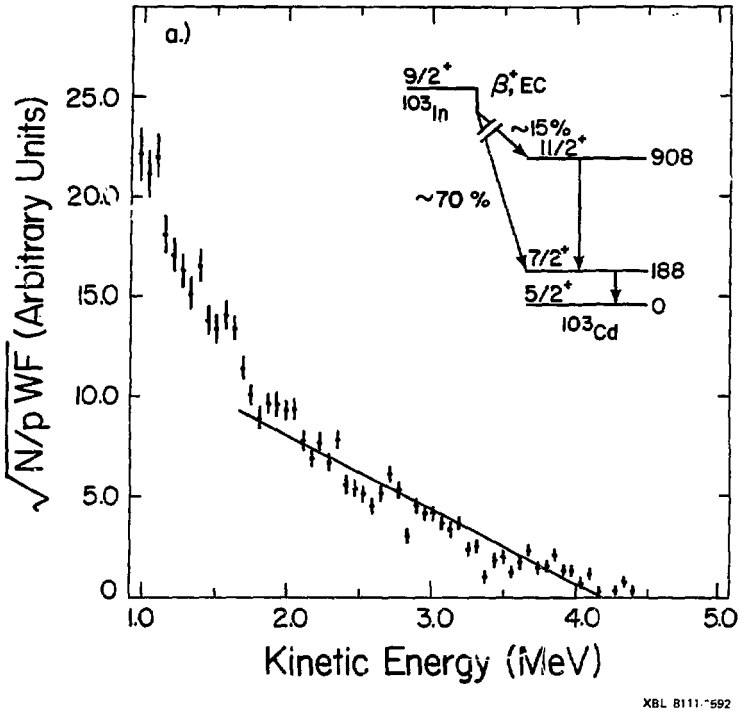

Figure 4-3. The Fermi-Kurie plot and partial decay scheme for ^{103}In.

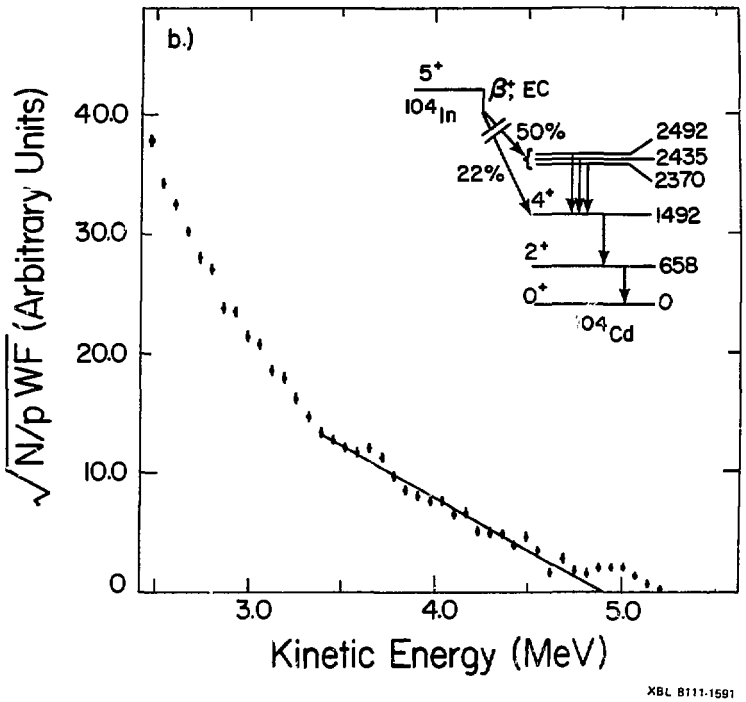

Figure 4-4. The Fermi-Kurie plot and partial decay scheme for ^{104}In.

with the 658 keV and 834 keV γ-rays yield, within errors, the same β-endpoint energy, but have lower statistics.

According to Wischnewski et al. (Wi 80), about 27% of the ^{105}In β-decay feeds the first excited level at 131 keV in ^{105}Cd, while the next strongly fed levels, decaying to the 131 keV state, lie at 770 and 799 keV with β branches of 8% and 9%, respectively. The resulting partial decay scheme and Fermi-Kurie analysis of the positron spectrum in coincidence with the 131 keV γ-ray are shown in figure 4-5. Figure 4-2c shows the γ-spectrum obtained in coincidence with positrons from the decay of ^{105}In.

The measured β-endpoint energies, E_{MAX}, along with the γ-rays used for gating and the Q_{EC} values deduced are summarized in table 4-2 for $^{103-105}$In. In addition, the decay energies previously reported in the literature are included in the table for comparison. The decay energies obtained for $^{103-104}$In agree well with the literature values; for ^{103}In the uncertainty in the Q_{EC} value is substantially reduced. A Q_{EC} value for ^{105}In was not previously available.

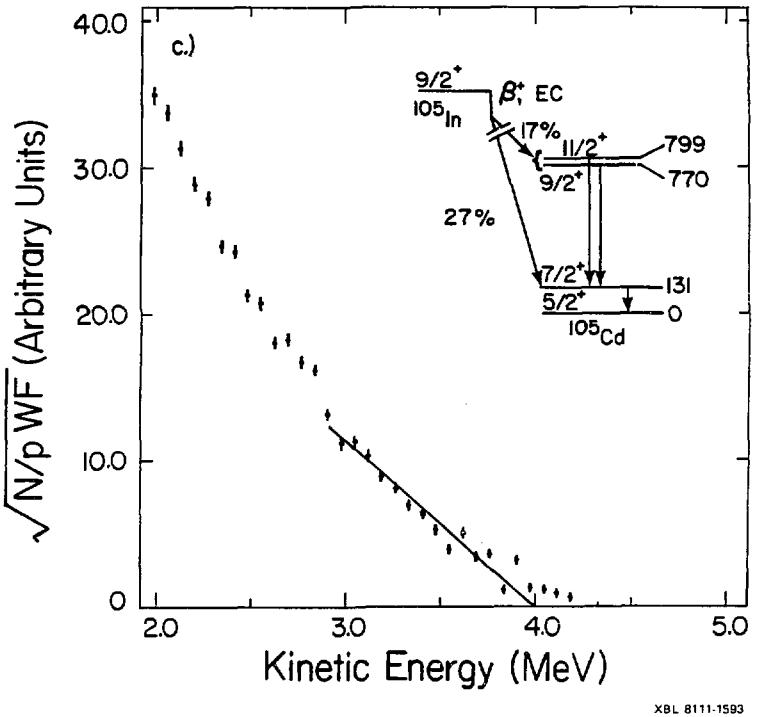

Figure 4-5. The Fermi-Kurie plot and partial decay scheme for ^{105}In.

V Discussion

Analysis of the decay energy measurements for $^{103-105}In$, reported here, can proceed following several model-independent or -dependent approaches, in order to investigate the behavior of the mass surface. Direct model-independent information on variations in the mass surface for these indium isotopes can be obtained from an examination of the Q_{EC} and neutron binding energy systematics in the vicinity of the measured nuclei. A comparison with the available mass theories can evaluate the reliability of these models in predicting the curvature of the mass surface. Conversion of Q_{EC} values to mass excesses using the known masses of the cadmium isotopes also provides a direct comparison of the absolute mass excesses with the model mass predictions.

The Q_{EC} systematics of the odd Z nuclei between A=90 and A=125 are graphed using a modified Way-Wood (Wa 54) diagram in figure 5-1. This figure is divided into part (a), covering the even N nuclei, and part (b), covering the odd N nuclei, because of the differences in Q_{EC} arising from the neutron pairing energy. (Note the higher Q_{EC} for the odd N nuclei resulting from the pairing of an odd proton and removal of an odd neutron in the decay to the daughter.) Both figures clearly illustrate the proton shell closure at Z=50 by the discontinuity in the isotone lines, and to a lesser extent the Z=40 proton subshell closure. The N=50

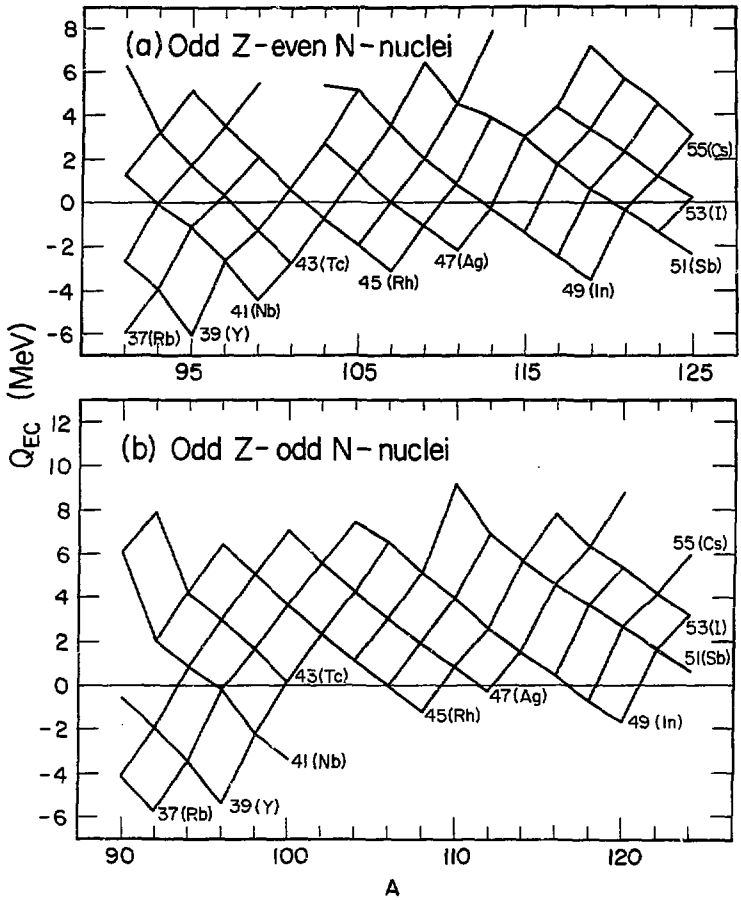

Figure 5-1. Modified Way-Wood diagrams which show Q_{EC} (MeV) versus A for a) odd Z-even N nuclei from A = 91 to 125 and b) odd Z-odd N nuclei from A = 90 to 124. Z = 40 and 50 shell closures are visible.

shell closure is also evident though the figures do not extend to quite a low enough A to permit observation of the systematic behavior.

The Q_{EC} values for the decays of $^{103-105}In$ are included in figure 5-1 and show a noticeable deviation from systematics, especially for the lightest indium isotopes. Figure 5-1a indicates that the odd-A indium isotopes follow the Q_{EC} surface as expected out to ^{105}In, but then suddenly deviate at ^{103}In. To a lesser extent the same behavior is observed in figure 5-1b with a slight deviation observed for ^{104}In. In both instances, the expected decay energies are larger than are actually observed.

To obtain a more quantitative understanding of this deviation, the differences between the measured decay energies and the predictions derived from selected mass models for the neutron-deficient indium isotopes are depicted graphically in figure 5-2. To observe more easily the systematic trends, this comparison is extended to ^{110}In. [The decay energies for $^{106-110}In$ are adopted from Wapstra and Bos (Wa 77]. Each arrow in the figure is labeled by a number corresponding to the prediction of a given model. Besides the different mass formulae presented in (Ma 76), the modified liquid drop calculations of Möller and Nix (Mo 80c) are also included.

Figure 5-2 shows that the results of the shell model calculations of Liran-Zeldes (Ma 76d) and the mass formulae,

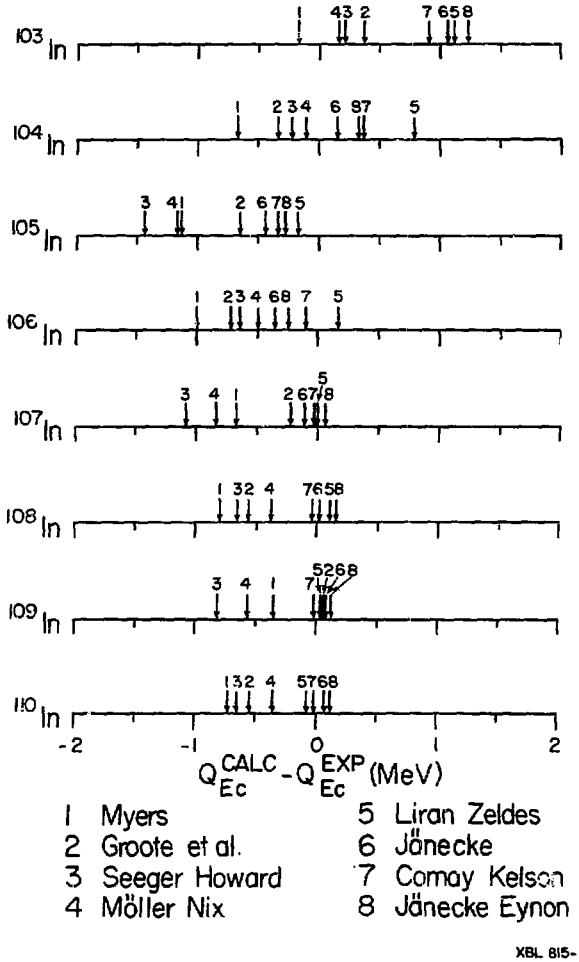

Figure 5-2. Comparison of the experimental Q_{EC} values with the predictions of several model mass formulae for $^{103-110}$In. (See text for details.)

based on the Garvey-Kelson type relationships, of Jänecke (Ma 76c), Comay-Kelson (Ma 76f) and Jänecke-Eynon (Ma 76g) reproduce very well the measured decay energies for $^{105-110}$In. In this region, the Droplet model predictions of Myers (Ma 76a), and Groote et al. (Ma 76b), and the modified liquid drop model predictions of Seeger and Howard (Ma 76c), and Möller and Nix (Mo 80c) are systematically too poorly bound. Beginning with ^{104}In and continuing to ^{103}In, both types of mass theories exhibit a sudden downward shift of 1 MeV so that the Liran-Zeldes and Garvey-Kelson type relationships now predict a Q_{EC} which is 1 MeV too large, while those based on a modified liquid drop model (here after referred to as MLD models) are at this point more accurate.

The mass excesses of $^{103-105}$In, deduced from the measured Q_{EC} values using the accurately known cadmium masses (Hu 78, Pa 78, Pl 79, Pl 81), are listed in table 5-1. A direct comparison of the experimental masses with the different model mass predictions is also included in the table. From table 5-1, it is apparent that none of these mass formulae adequately predicts the experimentally-observed mass behavior for $^{103-105}$In. Mass theories which reproduce the experimental mass of ^{105}In (i.e. Groote et al., Liran-Zeldes, Comay-Kelson and Jänecke-Eynon) place the ^{103}In mass 1 MeV higher than is experimentally observed.

Given the sudden deviation in the ^{103}In experimental

Table 5-1. Summary of Experimental Mass Excesses and Comparison with Different Model Mass Predictions

Nuclide	Mass Excess	$M_{exp}-M_{calc}$ (MeV)							
		a	b	c	d	e	f	g	h
^{103}In	-75.24±0.13	0.67	-1.20	0.76	-0.73	-1.20	-0.81	-0.81	-1.13
^{104}In	-76.30±0.14	1.01	-0.49	1.30	-0.10	-0.57	0.19	-0.06	-0.18
^{105}In	-79.20±0.13	1.23	-0.08	1.90	0.46	0.26	0.57	0.38	0.26

a) Myers (Ma 76a), b) Groote et al. (Ma 76b); c) Seeger-Howard (Ma 76c); d) Möller-Nix (Mo 80c); e) Liran-Zeldes (Ma 76d); f) Jänecke (Ma 76e); g) Comay-kelson (Ma 76f); h) Jänecke-Eynon (Ma 76g).

mass compared to these predictions and also its proximity to the double shell closure at ^{100}Sn, a comparison of the systematics of the ground state mass behavior for the very neutron-rich indium isotopes near the shell closure at N=82 is of related interest. Aleklett et al. (Al 78) have studied the masses of $^{120-129}In$. For the mass excess of the closed neutron shell nucleus ^{131}In, a value of -68.55 ± 0.24 MeV can be calculated from the recently reported decay energies of ^{131}In (De 80) and ^{131}Sn (Ke 79) and the measured mass of ^{131}Sb (Lu 77). [The masses of the indium isotopes, not explicitly mentioned here, were adopted from (Wa 77).]

In figure 5-3, the experimental indium masses for isotopes between shell closures at N=50 and N=82 are compared to the predictions of selected, representative mass theories. The lower part of this figure compares shell and independent-particle mass formulae; the upper part compares different MLD model predictions. The central part of the mass data between N=57 and N=76 is reproduced by the shell model of Liran-Zeldes (Ma 76a) and the mass formulae based on the Garvey-Kelson relations (Ma 76e, Ma 76f, Ma 76g); the root-mean-square (rms) deviation of theory from experiment in this region is less than 200 keV for each of these mass models. Approaching the closed N=82 shell, the different mass predictions diverge slowly. The model of Comay-Kelson (Ma 76f) exhibits the best predictive qualities taking into

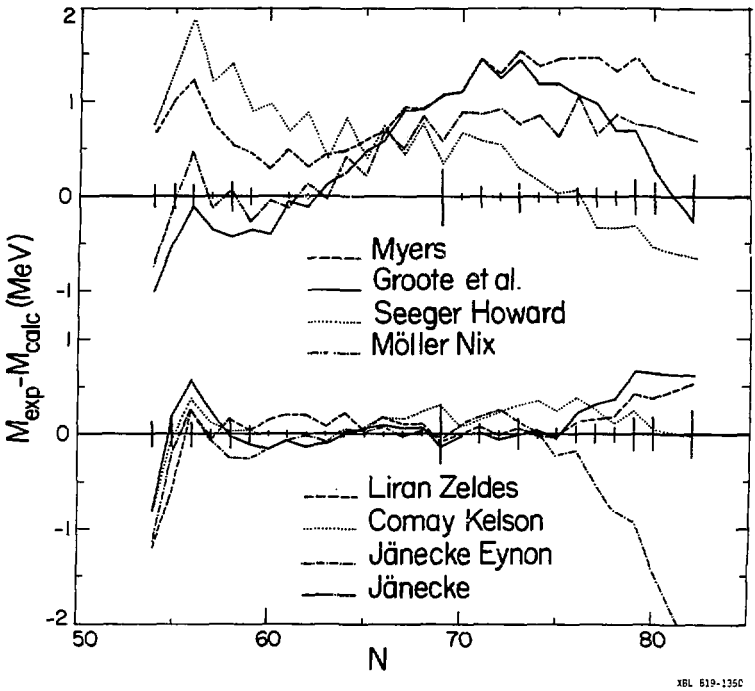

Figure 5-3. Comparison of the experimental masses of all the known indium isotopes with the predictions of several model mass formulae.

account all of the indium data; the rms deviation from all the measured masses is only 240 keV. For the models of Liran-Zeldes (Ma 76d), Jänecke (Ma 76e), and Jänecke-Eynon (Ma 76g), the corresponding values are 320, 320, and 630 keV, respectively.

From figure 5-3, it is also clear that the different MLD models, considered in this work, do not predict the masses of the indium isotopes in the region near stability with the same accuracy as the Liran-Zeldes mass formula and the models based on the Garvey-Kelson type mass relations. One should remember, however, that the number of input parameters used for the MLD models is far fewer than for the other mass formulae (see table 2-2). Near the N=50 and N=82 closed shells, the differences between the experimental and calculated mass values for the MLD models and Garvey-Kelson type mass formulae are of the same order. Among the MLD models, the best fit to the experimental data over the known mass range is obtained with the model of Möller and Nix; the rms deviation is 630 keV. In the case of the mass formulae of Myers, Groote et al., and Seeger and Howard, this deviation is 1060, 820, and 780 keV, respectively. Finally, the differences between the experimental masses and the various MLD model predictions also show the sharp, systematic drop at mass 103. Table 5-2 summarizes the comparison with the various mass predictions over the known indium masses, giving the root-mean-square (rms) deviation

Table 5-2. Summary of RMS Deviations of the Different Model Mass Predictions from the Experimental Mass Excesses

Model (Ma 76, Mo 80c)	RMS Dev. (keV)
Myers	1060
Groote et al.	820
Seeger-Howard	780
Möller-Nix	630
Liran-Zeldes	320
Jänecke	320
Comay-Kelson	240
Jänecke-Eynon	630
Experimental error	110

of each mass prediction from the experimentally measured indium masses. Also included, as a reference, is the rms error associated with the experimental masses in order to comprehend better the predictive powers of mass formulae.

An examination of single- and two-nucleon separation energies can highlight systematic variations of the mass surface in a model-independent way. Figure 5-4a shows the behavior of the single-neutron separation energy, S_n, as a function of the neutron number for the indium isotopes. Besides the normal odd-even oscillations, the S_n plot exhibits an irregular drop for N=55 and N=56. Both S_n values are about 0.5 MeV lower than those estimated from the systematics of Wapstra and Bos (Wa 77), which are indicated in the figure by dashed lines. Since the mass of ^{105}In is in agreement with the estimate of Wapstra and Bos, the observed deviations reflect the fact that the masses of ^{104}In and ^{103}In are, respectively, 0.5 and 1.0 MeV lower than expected from systematics. From figure 5-4a it is apparent that a similar effect is not present for the neutron-rich indium isotopes near the closed N=82 shell.

Since the neutron pairing energy is closely related to a quantity Δ_n, which can be derived from single neutron separation energies using the relationship (Ni 61)

$$\Delta_n = [(-1)^N/4][2S_n(N,Z) - S_n(N+1,Z) - S_n(N-1,Z)] \quad (5\text{-}1)$$

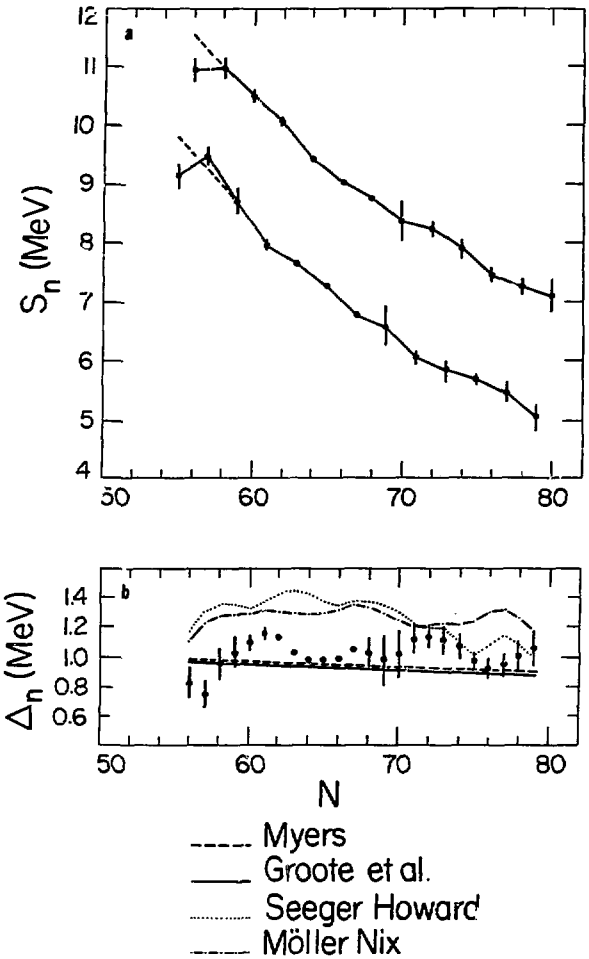

Figure 5-4. a) Plot of single-neutron separation energies versus neutron number for even and odd N isotopes. Dotted lines are single-neutron values expected from Wapstra and Bos (Wa 77) systematics. b) Plot of experimental and MLD model predicted Δ_n values versus neutron number.

a comparison of the experimental behavior of Δ_n with the values of the different MLD models is informative. The variation of Δ_n for the measured indium isotopes is presented in figure 5-4b by the dots with the error bars. Excluding the values for N=56 and N=57, where S_n shows an irregular behavior, Δ_n is found to fluctuate between 0.95 and 1.15 MeV resulting in a mean value Δ_n of 1.04±0.06 MeV. The comparison with the Δ_n values of the models of Myers (Ma 76a) and Groote et al. (Ma 76b) indicates that the pairing terms in these models, which both basically employ the phenomenological $A^{-1/2}$ mass dependence (see sections II-b2 and II-B3d), are slightly too low. These mass formulae predict mean values for Δ_n of 0.94 and 0.92 MeV, respectively. On the other hand, the models of Seeger and Howard (Ma 76c) and Möller and Nix (Mo 80c), which use the BCS formalism to calculate the pairing correction (see sections II-B3e and II-B3f), yield pairing terms which are too high. Mean values for Δ_n of 1.26 and 1.28 MeV, respectively, are obtained using these macroscopic-microscopic approaches.

The two-neutron separation energies S_{2n} are plotted in figure 5-5 versus neutron number in the region of the indium isotopes near the closed N=50 shell. In the S_{2n} plots, the odd-even oscillations are filtered out. The recently published masses of ^{97}Pd (Go 80), ^{98}Pd (Th 78), ^{100}Ag (Ha 80), ^{103}Cd (Pa 78), ^{104}Cd (Pl 79, Pl 81), and ^{106,108}Sn

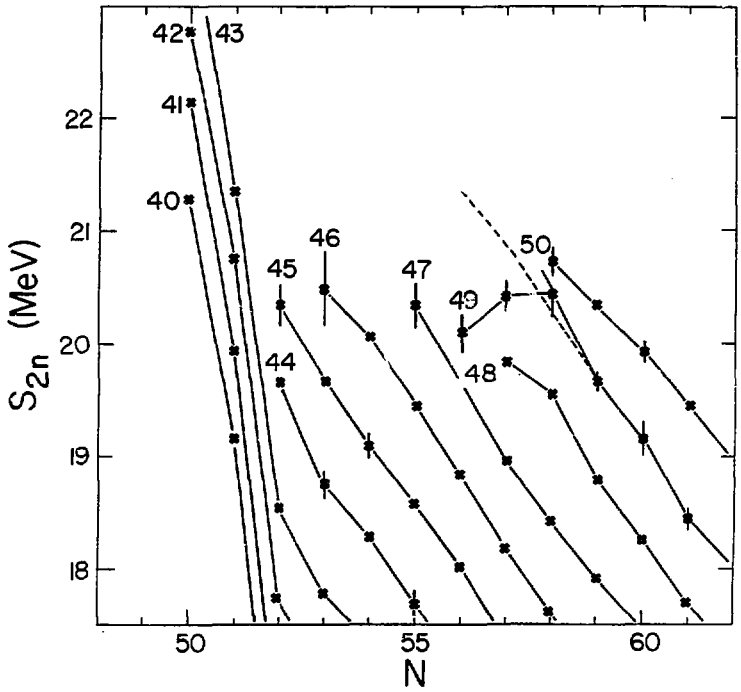

XBL 815-818

Figure 5-5. Plot of the experimental two-neutron separation energies versus neutron number for elements with Z = 40 to 50 near the closed neutron shell at N = 50. (See text for details.)

(Pl 79, Pl 81) were also used to calculate S_{2n} values. The dashed line in the figure indicates the S_{2n} behavior according to the systematics of Wapstra and Bos (Wa 77). Except for the well known discontinuity corresponding to the N=50 closed shell, figure 5-5 only shows a strong deviation from the systematics for the neutron-deficient indium isotopes.

The observed irregular mass behavior of ^{103}In and ^{104}In might easily be interpreted as due to a sudden change in nuclear deformation as is present in the rare earth region (Du 69). However, the proximity to the doubly closed shell at ^{100}Sn and ancillary evidence strongly suggest that an alternative interpretation is necessary. The reported systematics of the 2^+ and 4^+ levels in the light even cadmium isotopes (Be 81a, Be 81b) lead to a decrease in β_2, which measures the degree of prolate deformation, with decreasing N from $\beta_2 = 0.17$ for ^{110}Cd to $\beta_2 = 0.10$ for ^{102}Cd. This result plus the Hartree-Fock calculations of Meyer et al. (Me 79) strongly indicates that the cadmium isotopes are becoming more spherical as N approaches 50, which is consistent with a double shell closure. Less compelling, because of the large experimental uncertainties, are the recent Q_α systematics presented by Plochocki et al. (Pl 79) which suggest the proton shell strength is getting stronger as ^{100}Sn is approached. Attributing the extra binding energy of ^{103}In and ^{104}In to such an increase in the

proton shell strength must await a further extension of the experimentally known nuclidic mass surface towards ^{100}Sn. Such mutual enforcement of proton and neutron magicity has been discussed by several authors (Sc 79, Ze 79, Ze 81) and is clearly present in the lead region (Sc 79). Caution is necessary in making the same conclusion for the indium isotopes since exceptions occur, as in the case of the neutron rich indium isotopes, near the doubly closed shell nucleus ^{132}Sn.

VI Summary and Conclusions

Addition of a β-γ coincidence detector station for use with the RAMA separator has been described. This detector station consists of a scintillator telescope for positron (electron) energy measurements and a Ge(Li) counter for detection of the coincident γ-rays. Associated developments also discussed include the building of a fast tape transport for the collecting and shuttling of mass separated sources and the writing of an analysis code for the determination of β-endpoint energies.

Initial β-γ coincidence experiments using RAMA have led to the β-endpoint determination of the $^{103-105}$In Q_{EC} decay energies which are 5.38 $\pm$ 0.13 MeV, 7.42 $\pm$ 0.14 MeV, and 5.14 $\pm$ 0.13 MeV, respectively. Furthermore, the β-decay of ^{102}In has been observed and a half-life measured, verifying its recent discovery by Béraud et al. (Be 71b).

Comparison of the indium masses, which have been calculated from the Q_{EC} measurements and the known cadmium ground state masses, with the predictions of several different mass formulae show a marked deviation from systematics with ^{103}In better bound by about 1 MeV than expected. More model independent analyses based on the behavior of the Q_{EC} surface and the single- and two-neutron separation energies for the very neutron-deficient indium isotopes further reveals that both the ^{103}In and ^{104}In masses are lower than expected from the mass systematics of the heavier indium and neighboring isotopes. Attributing

these observed deviations to the nearby Z=N=50 shell closure will require more investigations of the mass surface in this region.

An extension of these experiments further away from the valley of β-stability using the same techniques will depend on how rapidly the cross sections decrease. For ^{103}In, the observed counting rate of 2 counts/min. permits a rough approximate estimation of the cross section for the ^{92}Mo(^{14}N,3n)^{103}In reaction to be 200μb. Studies of reaction products with even smaller cross sections might be permitted by relaxing the β-γ coincidence requirement since, for example, the expected large decay energy available to ^{102}In should distinguish those positrons originating from its decay. Improvements to increase the RAMA efficiency will greatly aid future studies; however, use of heavier projectile beams will ultimately provide the best chance of reaching the most neutron deficient medium-mass isotopes. Recently, the GSI on-line separator collaboration has observed β-delayed protons arising from the decays of ^{103}Sn (∿1mb cross section) and ^{105}Sn (∿30mb cross section) (Ti 81) which were produced in the ^{58}Ni on ^{54}Fe and ^{58}Ni on ^{50}Cr reactions.

Of course, the use of RAMA for β-γ coincidence studies is not restricted to nuclei near ^{100}Sn. Many other neutron-deficient nuclei, especially the T_z = -1/2 and -1 nuclei in the A=40 to 70 region, are quite poorly characterized.

These nuclei are amenable for spectroscopic studies with RAMA because of the suitable particle beams available at the 88-inch cyclotron. Half-life measurements, branching ratio measurements, and β-endpoint determinations, which should all be obtainable, will enable the calculation of Gamow-Teller matrix elements, log *ft*'s, and masses.

Acknowledgements

Though only one name appears on the cover of this thesis, the ability to successfully complete an experimental program depends on many individuals which I would like now to sincerely thank.

My first thanks goes to the entire crew, of the 88-inch cyclotron; the unsung heroes who never are recognized except in the thesis of graduate students. Without their dedication, an experiment would just be a "twinkle in the experimenter's eye." I especially want to thank Carol Adams for all her lively advice, and Roy Burton for teaching me the fine points of drafting.

I would like to thank Professor Joseph Cerny, my research advisor, for believing in small undergraduate colleges and thereby providing me with the opportunity to do forefront nuclear physics research. Joe's ability to remain excited even when RAMA was less than cooperative especially helped me to persevere.

To All graduate students and pseudo-graduate students including: Alden Bice, Claude Ellsworth, Roger Parry, Dieter Stahel, and Dave Vieira for all their camaraderie and help. I would especially like to thank Mike Cable for all the useful discussion and sometimes not so useful (but memorable) bullshit sessions.

During my tenure many guests visited our group and contributed greatly to my understanding of β-endpoint measurements. I would like to especially thank Professor

Hugh Evans, who figured out how to get a signal out of the β-telescope, Dr. Juha Äystö, who accidently stumbled into the indium experiments, Dr. Peter Haustein, who thought he would never see the last of a certain tape drive, and Dr. Hubert Thierens, who finally determined what constitutes a good set of β calibration nuclei.

In addition several members of the laboratory, not directly associated with the 88-inch cyclotron, greatly helped during various stages of the indium research. These include: Dr. Creve Maples, who got me interested in interactive computer programs (and who taught me that no matter how often a program is revised, it is never completed), Prof. Stanley Prussin, who taught me common sense nuclear physics, Dr. George Gabor, who helped design and build the β-telescope, and Dr. William Myer, who greatly increased my understanding of mass models.

Behind every dedicated scientist, there is a supporting force which keeps him honest. I would like to thank Dennis Moltz for not only providing a mass separator, but for also introducing me to his sister, Laura, who somehow ended up as my wife. Laura has kept me honest to my goals and principles, and never let a dull day pass even when everything else seemed to be crawling along.

Finally, I would like to thank RAMA for all of those 4 am breakdowns that kept me awake at night and who taught me (several times) what cleaning up after Noah's flood must

have been like.

This work was supported by the Director, U.S. Office of Energy Research, Division of Nuclear Physics of the Office of High Energy and Nuclear Physics, and by Nuclear Sciences of the Basic Energy Sciences Program of the U. S. Department of Energy under Contract No. W-7405-ENG-48.

Appendix A - Design of a multiple-capillary, multiple-target system

Introduction of the multiple-capillary, multiple-target system has greatly increased the scope of experiments which are feasible with RAMA. The factors influencing the number and spacing of both capillaries and targets in order to maximize the yield are now briefly described. The thickness and spacing of the targets is governed by the recoil range of the nuclide of interest in each target and in the helium gas. Maximum yield (i.e., maximum number of recoils per unit volume) is attained with each target one recoil range thick and spaced one recoil range (in helium) apart. The number of targets is set by the width of the reaction excitation function since approximately equal numbers of nuclides should be produced in each target. For the heavy ion beams used in studying $^{102-105}$In, two targets were the maximum allowable because of the large energy drop per target.

The number and spacing of the small capillaries is determined largely by the increased time needed to collect and transport the recoils, with increasing number of capillaries. Each capillary collects recoils over $\sim$1 cm^3 region which sets the closest spacing between them. The total transport time, t_d, may be subdivided into the collection time, t_{col}, the transport time through the multiple capillaries, t_{mc}, and the transport time through the main capillary, t_m (Mo 80b). The first two terms increase linearly with the number of small capillaries.

Equation (A-1) gives the explicit dependence of t_d assuming the approximation $t_m = 2L/3V_o$ from (We 75).

$$
\begin{aligned}
t_d &= t_{col} + t_{mc} + t_m \\
&= N\Delta V/Q + L_{mc}/V_{mc} + 2L/3V_o \\
&= (1/Q)(N\Delta V + N\pi L_{mc}D_{mc}^2/4 + \pi L_m D_m^2/6)
\end{aligned}
\qquad \text{(A-1)}
$$

N = number of capillaries
ΔV = active coll. vol./cap.
Q = flow rate
L_{mc} = ave. mult. cap. length
$V_{mc} = 4Q/N\ D_{mc}^2$
= ave. velocity in mult. cap.
D_{mc} = dia. of multi. cap. tube
L_m = Length of main cap.
$V_o = 4Q/\ D_m^2$
= init. vel. in main cap.
D_m = diameter of main cap.

The total yield through the system is given then by

$$\text{YIELD} = AN\Delta V_o \exp[-\ln 2 x (t_d/t_{1/2})] \qquad \text{(A-2)}$$

which depends linearly on N and exponentially on $-t_d/t_{1/2}$ as expected, where $t_{1/2}$ is the half life of the nuclide of interest. This equation is plotted in figure A-1 as a function of N and $t_{1/2}$. For the 1.27 mm i.d. main capillary used in the indium experiments the yield is observed to increase approximately linearly for $t_{1/2}$ greater than a couple of seconds. This observation resulted in the use of six capillaries spaced 6 mm apart (closest spacing) per target. Note that figure A-1 indicates that the yield can drop with increasing number of capillaries if $t_{1/2}$ is short enough. This problem was of no concern for the indium

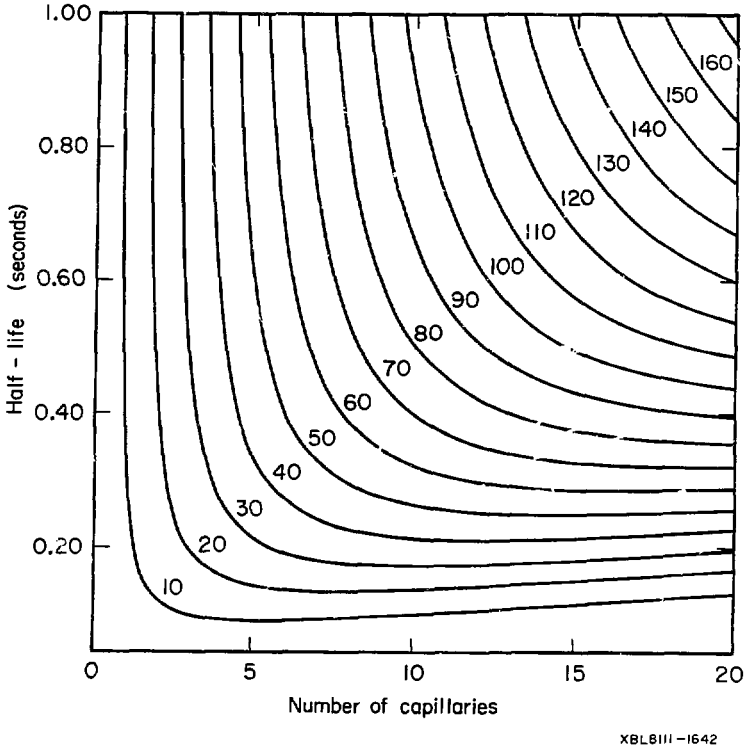

Figure A-1. Contour plot (Wo 81b) of total yield from helium-jet as a function of the number of capillaries and the half-life of the transported activity.

experiments since the shortest lived nuclide (^{102}In, $t_{1/2}$= 24 sec) possessed a reasonably long half-life.

Appendix B - Tape transport cycling interval

Yield optimization of the observed activity requires careful selection of the tape transport cycling interval, T_I. The total interval can be divided into two parts: the transport time, T_T, and the tape collection, T_C, or tape observation time, T_O. (Note that these two are equal, since one sample is collected while the previous one is observed.) Since T_T is fixed for the tape drive at 125 milliseconds, the problem is reduced to determining T_C. From elementary radioactive decay kinematics, the net rate of deposition of activity, dN/dt, at the collection point is given by

$$dN/dt = A - \lambda N \qquad \text{(B-1)}$$

where A is the RAMA rate of production of the activity and λ is the activity's decay constant. The total number of nuclei collected is thus given by

$$N_C = (A/\lambda)e^{-\lambda T_C}(e^{\lambda T_C}-1) \qquad \text{(B-2)}$$

During the transport time T_T the nuclei simply decay, thus the remaining number of nuclei is given by

$$N_O = N_C e^{-\lambda T_T} \qquad \text{(B-3)}$$

The maximum number of nuclei which are observable is simply

then the number at the beginning of the observation period, N_o, minus the number, N_F, at the end.

$$N_F = N_o e^{-\lambda T_c}$$
$$N_o - N_F = (A/\lambda) e^{-\lambda T_T} (1 - e^{-\lambda T_c})^2 \qquad \text{(B-4)}$$

The tape transport efficiency is given by $N_o - N_F$ divided by the total number of nuclides which would be observed if the detector were looking directly at the collection spot during a time T_I. Maximization of this efficiency with respect to T_c, then gives the optimum cycling interval T_I.

$$\text{Efficiency} = (1/\lambda) e^{-\lambda T_T} (1 - e^{-\lambda T_c})^2 / (T_c + T_t) \qquad \text{(B-5a)}$$
$$1 + 2\lambda (T_c + T_T) = e^{-\lambda T_c} \qquad \text{(B-5b)}$$

Equation (B-5b) must be solved numerically to obtain T_c. For $t_{1/2} >> t_T$ the optimum cycle interval t_I is approximately $1.8 \times t_{1/2}$ and the efficiency relative to counting on the focal plane is 41%. Finally, the relative efficiencies of observing one activity versus another produced by RAMA with the same yield is given by:

$$\text{Eff}_1/\text{Eff}_2 = (\lambda_2/\lambda_1) e^{-T_T(\lambda_1 - \lambda_2)} (1 - e^{-\lambda_1 T_c})^2 \times (1 - e^{-\lambda_2 T_c})^{-2} \qquad \text{(B-6)}$$

Appendix C - Endpoint error analysis (derivations)

Equations (3-6) and (3-7) are quoted as the statistical and energy calibration errors, respectively, in section III-D2. The derivations of these two equations are now given using the formalism of Bevington (Be 69b); note however, that A and B, the slope and intercept of a line, are interchanged from Bevington's notation. Equation (3-6) was originally derived by (Re 78) and is included here for completeness. Since the endpoint, W_o, equals -B/A and σ_{FK}^2 is given by:

$$\sigma_{FK}^2 = \sum_j \sigma_Y^2 (dW_o/dYF_j)^2 \qquad \text{(C-1)}$$

where YF_j is just the equation of the line fitted to the Fermi-Kurie plot

$$YF_j = AxW_j + B \qquad \text{(C-2a)}$$
$$= f_A(W_i, Y_i)W_j + f_B(W_i, Y_i) \qquad \text{(C-2b)}$$

and Y_i is just

$$Y_i = (N_i/P_iF_iW_i)^{1/2} \qquad \text{(C-3)}$$

A and B are clearly functions of W_i and Y_i, as is evident in equation (C-2b), since they are determined by the least-squares fit to the set of ordered pairs (W_i, Y_i) and are given on page 107 of Bevington:

$$f_A(W_i,Y_i) = \Delta^{-1}\{\Sigma\sigma_{Y_i}^{-2}\,\Sigma(W_iY_i/\sigma_{Y_i}^2) - \Sigma(W_i/\sigma_{Y_i}^2)\,\Sigma\,(Y_i/\sigma_{Y_i}^2)\} \qquad \text{(C-4a)}$$

$$f_B(W_i,Y_i) = \Delta^{-1}\{\Sigma\,(W_i^2/\sigma_{Y_i}^2)\,\Sigma\,(Y_i/\sigma_{Y_i}^2) - \Sigma\,(W_i/\sigma_{Y_i}^2)\,\Sigma\,(W_iY_i/\sigma_{Y_i}^2)\} \qquad \text{(C-4b)}$$

$$\Delta = \Sigma\sigma_{Y_i}^{-2}\,\Sigma\,(W_i^2/\sigma_{Y_i}^2) - [\,\Sigma\,(W_i/\sigma_{Y_i}^2)\,]^2$$

Using equations (C-2) and (C-4), (C-1) may now be calculated beginning with the calculation of dW_o/dYF_j,

$$dW_o/dYF_j = (B/A^2)\,(df_A/dY_j) + (-1/A)\,(df_B/dY_j) \qquad \text{(C-5)}$$

$$\sigma_{FK}^2 = A^{-2}\,\Sigma\,\sigma_{Y_i}^2\,[W_o(df_A/dY_j) + (df_B/dY_j)] \qquad \text{(C-6)}$$

$$W_o = -B/A$$

This expression may now be simplified by explicitly calculating df_A/dY_j and df_B/dY_j, using equation (C-4), giving equation (3-6) as desired:

$$\sigma_{FK}^2 = (1/A^2\Delta)\;\Sigma(W_j - W_o)^2/\sigma_{Y_j}^2 \qquad \text{(C-7)}$$

Calculation of equation (3-7), the energy calibration error, proceeds along similar lines, but now $\sigma_{W(calib)}$ is given by

$$\sigma_{W(calib)}^2 = \Sigma\,\sigma_{W_i}^2(dW_c/dW_i)^2 + \Sigma\,\sigma_{X_i}^2(dW_c/dX_i)^2 \qquad \text{(C-8)}$$

since the calibration is a function of both W_i, the

literature endpoints, and X_i, the corresponding x-axis intercept channel number,

$$W_o = A_c X_o + B_c. \qquad \text{(C-9a)}$$
$$= f_{A_c}(W_i, X_i) X_o + f_{B_c}(W_i, X_i) \qquad \text{(C-9b)}$$

Using equation (C-8) and (C-9), the quantities dW_c/dW_i and dW_c/dX_i can be calculated to give an equation for $\sigma_{W(calib)}^2$ analogous to (C-6):

$$dW_c/dW_i = X_o(df_{A_c}/dW_i) + (df_{B_c}/dW_i) \qquad \text{(C-10a)}$$
$$dW_c/dX_i = X_o(df_{A_c}/dX_i) + (df_{B_c}/dX_i) \qquad \text{(C-10b)}$$
$$\sigma_{W(calib)}^2 = \Sigma\{\sigma_{W_i}^2[X_o(df_{A_c}/dW_i)+(df_{B_c}/dW_i)]^2 + \sigma_{X_i}^2[X_o(df_{A_c}/dX_i)+(df_{B_c}/dX_i)]^2\} \qquad \text{(C-10c)}$$

and which corresponds to equation (3-7) with $\sigma_{W_i} = \sigma_{lit_i}$, $\sigma_{X_i} = \sigma_{FK_i}$, $f_{A_c} = f_A$ and $f_{B_c} = f_B$. The partial differentials can be calculated using equations (C-4) as before, but with Y_i now replaced by W_i and W_i replaced by X_i; compare equations (C-2a) with (C-9a). This substitution does not lead to a simplified expression as appeared earlier and is included only for completeness and to indicate the major dependences.

$$calib^2 = \Sigma(\sigma_{X_j}/\Delta\sigma_j^2)^2\{X_o[W_j \Sigma\sigma_i^{-2} - \Sigma(W_i/\sigma_i^2)] + [2X_j \Sigma(W_i/\sigma_i^2) - \Sigma(X_i W_i/\sigma_i^2) - W_j \Sigma(X_i/\sigma_i^2)] - 2[X_j \Sigma\sigma_i^{-2} - \Sigma(X_i/\sigma_i^2)]\}^2 \qquad \text{(C-11a)}$$

$$+\Sigma(\sigma_{W_i}/\Delta\sigma_j^{\,2})^2\{X_o[X_j\Sigma\sigma_i^{\,-2}-\Sigma(X_i/\sigma_i^{\,2})]$$
$$+[\Sigma(X_i^{\,2}/\sigma_i^{\,2})-X_j\Sigma(X_i/\sigma_i^{\,2})]\}^2$$

where

$$\sigma_j^{\,2} = \sigma_{X_j}^{\,2} + \sigma_{W_j}^{\,2} \qquad \text{(C-11b)}$$

and Δ corresponds to Δ in equation (C-4c) with x_i substituted for W_i.

Footnotes

1. Havar is the trade name for a metal alloy consisting of Co (42.5%), Ni (13.0%), Cr (20.0%) and Fe (17.9%) with a density of 8.3 gm/cm^3 which is manufactured by the Metals Division of the Hamilton Watch Co., P.O. Box 1609, Columbia Ave., Lancaster, PA 17604.

2. Tube Sales, 2211 Tubeway, Los Angeles, CA 90040.

3. Leybold-Heraeus Vacuum Products, Inc., 5700 Mellon Rd., Export, PA 15632.

4. Tungsten wire for filaments manufactured by Lamp Parts Dept. of the Westinghouse Electric Co., Westinghouse Plaza, Bloomfield, NJ 07003.

5. Tungsten tubing for outer cathode manufactured by Ultramet, 12173-5 Montague St., Pacoma, CA 91331.

6. HP grade boron nitride obtained from Electric Products Division (Domestic Section) of the Carborundum Co., P.O. Box 577, Niagra Falls, NY 14302.

7. Impolene is a trade name for a polyallomer tubing manufactured by the Imperial-Eastman Co., 6300 West Howard St., Chicago, IL 60648.

8. RMB miniature ball bearings distributed by Landis & Gyr, Inc., 4 Westchester Plaza, Elmsford, NY 10523.

9. Dow Corning Co., Midland, MI 48640.

10. RCA Co., Solid State Division, 4827 Sepulveda, Sherman Oaks, CA 90045.

11. Ortec Inc., 100 Midland Rd., Oak Ridge, TN 37830.

12. ModComp is the registered trademark of the Modular Computer Corporation, 1650 West Mcnab, Fort Lauderdale, FL 33310.

REFERENCES

(Al 78) K. Aleklett, E. Lund and G. Rudstam, Phys. Rev. C18, 462 (1978).

(Ay 79) J. Äystö, D. M. Moltz, M. D. Cable, R. D. von Dincklage, R. F. Parry, J. M. Wouters and J. Cerny, Phys. Lett. 82B, 43 (1979).

(Ay 81) J. Äystö, M. D. Cable, R. F. Parry, J. M. Wouters, D. M. Moltz, and J. Cerny, Phys. Rev. C23, 879 (1981).

(Ba 77) G. Baym, Lectures on Quantum Mechanics, (W. A. Benjamin Inc., Reading, Massachusetts, 1977) p. 251.

(Be 36) H. A. Bethe and R. F. Bacher, Rev. Mod. Phys. 8, 82 (1936).

(Be 69a) E. Beck, Nucl. Instr. Meth. 76, 77 (1969).

(Be 69b) P. R. Bevington, Data Reduction and Error Analysis for the Physical Sciences, (McGraw Hill, New York, 1969) chapters 5 and 6.

(Be 79) W. Benenson and E. Kashy, Rev. Mod. Phys. 51, 527 (1979).

(Be 81a) R. Béraud, J. Tréherne, A. Charvet, R. Duffait, A. Emsallem, J. Genevey, A. Gizon, J. Gizon and M. Meyer, in Proceedings of the Fourth International Conference on Nuclei Far From Stability, June 7-13, 1981, Helsingor, Denmark, p. 692.

(Be 81b) R. Béraud, J. Tréherne, A. Charvet, R. Duffait, J. Genevey, A. Gizon, J. Gizon and M. Meyer, Z. Physik A299, 279 (1981).

(Bl 52) J. M. Blatt and V. F. Weisskopf, Theoretical Nuclear Physics, (John Wiley and Sons, New York, 1952) p. 682.

(Bo 72) M. Bosterli, E. O. Fiset, J. R. Nix and J. L. Norton, Phys. Rev. C5, 1050 (1972).

(Ca 63) D. C. Camp and L. M. Langer, Phys. Rev. 129, 1782 (1963).

(Ce 74) J. Cerny, N. A. Jelley, D. L. Hendrie, C. F. Maguire, J. Mahoney, D. K. Scott and R. Weisenmiller, Phys. Rev C10, 2654 (1974).

(De 80) L. E. De Geer and G. B. Holm, Phys. Rev. C22, 2163 (1980).

(Du 69) H. E. Duckworth, R. C. Barber, R. van Rookhuysen, J. D. Macdougall, W. McLatchie, S. Whineray, R. L. Bishop, J. O. Meredith, P. Williams, G. Southon, W. Wong, B. Hogg and M. E. Kettner, Phys. Rev. Lett. 23, 592 (1969).

(Ep 79) M. Epherre, G. Audi, C. Thibaut, R. Klapisch, G. Huber, F. Touchard and H. Wollnik, Phys. Rev. C19, 1504 (1979).

(Fe 34) E. Fermi, Z. Physik 88, 161 (1934).

(Ga 36) E. Gamow and E. Teller, Phys. Rev. 49, 895 (1936).

(Ga 66) G. T. Garvey and I. Kelson, Phys. Rev. Lett. 16, 197 (1966).

(Ga 69a) G. T. Garvey, W. J. Gerace, R. L. Jaffe, I. Talmi and I. Kelson, Rev. Mod. Phys. 41, S1 (1969).

(Ga 69b) G. T. Garvey, Ann. Rev. Nucl. Sci. 19, 433 (1969).

(Go 71) N. B. Gove and M. J. Martin, Nucl. Data Tables 10, 205 (1971).

(Go 72) R. A. Gough, R. G. Sextro and J. Cerny, Nuclear Chemistry Division Annual Report for 1972, LBL-1666, 361, (unpublished).

(Go 80) H. Gokturk, N. K. Aras, P. Fettweis, P. Del Marmol, J. Vanhorenbeeck and K. Cornelis, Nucl. Phys. A344, 1 (1980).

(Ha 79) P. G. Hansen, Ann. Rev. Nucl. Part. Sci. 29, 69 (1979).

(Ha 80) H. I. Hayakawa, I. Hyman and J. K. P. Lee, Phys. Rev. C22, 247 (1980).

(Ha 81) J. H. Hamilton, prepared for Heavy Ion Collisions, edited by R. Bock, (North-Holland Publishing Co., Amsterdam, 1981).

(Hi 75) E. R. Hilf, H. V. Groote and K. Takahashi, Proceedings of the Fifth International Conference on Atomic Masses and Fundamental Constants, edited by J. H. Sanders and A. H. Wapstra, (Plenum Press, New York, 1975) p. 293.

(Hu 78) E. Huang, B. Pathak and J. K. P. Lee, Can. J. Phys. 56, 936 (1978).

(Ja 72) J. Jänecke and H. Behrens, Z. Physik 256, 236 (1972).

(Ja 74) J. Jänecke and H. Behrens, Phys. Rev. C9, 1276 (1974).

(Jo 81) B. Jonson, Nucl. Phys. A354, 77c (1981).

(Ke 66) I. Kelson and G. T. Garvey, Phys. Lett. 23, 689 (1966).

(Ke 79) U. Keyser, H. Berg, F. Münnich, K. Hawerkamp, H. Schrader, B. Pfeiffer and E. Monnand, Z. Physik A289, 407 (1979).

(Ko 65) E. J. Konopinski and M. E. Rose, in Alpha-, Beta- and Gamma- Ray Spectroscopy, edited by K. Siegbahn, (North-Holland Publishing Co., Amsterdam, 1965) p. 1338.

(Kr 79) H. J. Krappe, J. R. Nix and A. J. Sierk, Phys. Rev. C20, 992 (1979).

(La 67) Lawrence Berkeley Laboratory Publication No. 54 (1967).

(La 81) M. Lampton, Scientific American 245, 62 (1981).

(Le 78) C. M. Lederer and V. S. Shirley, Table of Isotopes Seventh Edition, (John Wiley and Sons, Inc., New York, 1978).

(Lh 78) G. Lhersonneau, G. Dumont, K. Cornelis, M. Huyse and J. Verplancke, Phys. Rev. C18, 2688 (1978).

(Li 62) H. J. Lipkin, Beta Decay for Pedestrians, (North-Holland Publishing Co., Amsterdam, 1962) chapter 3.

(Lu 77) E. Lund, K. Aleklett and G. Rudstam, Nucl. Phys. A286, 403 (1977).

(Ma 63) R. D. MacFarlane and R. D. Griffioen, Nucl. Instr. Meth. 24, 461 (1963).

(Ma 69) P. Marmier and E. Sheldon, Physics of Nuclei and Particles, vol. 1, (Academic Press, New York, 1969) p. 327.

(Ma 76) a) W. D. Myers, At. Data Nucl. Data Tables 17, edited by S. Maripuu, 411 (1976).
b) H. V. Groote, E. R. Hilf and K. Takahashi, ibid. 418.
c) P. A. Seeger and W. M. Howard, ibid. 428.
d) S. Liran and N. Zeldes, ibid. 431.
e) J. Jänecke, ibid. 455.
f) E. Comay and I. Kelson, ibid. 463.
g) J. Jänecke and B. P. Eynon, ibid. 467.

(Ma 79) C. C. Maples and J. Sivak, IEEE Transactions in Nuclear Science NS-26, 4409 (1979).

(Ma 81) G. Marguier, A. Charvet, J. Genevey, C. Richard-Serre, A. Knipper, G. Walter and the ISOLDE Collaboration, J. Phys. G: Nucl. Phys. 7, 101 (1981).

(Me 79) M. Meyer, J. Danniere, J. Letessier and P. Quentin, Nucl. Phys. A316, 93 (1979).

(Me 80) M. Meyer, R. Béraud, A. Charvet, R. Duffait, J. Tréherne and J. Genevey, Phys. Rev. C22, 589 (1980).

(Mo 79a) D. M. Moltz, J. Äystö, M. D. Cable, R. D. von Dinckalge, R. F. Parry, J. M. Wouters and J. Cerny, Phys. Rev. Lett. 42, 43 (1979).

(Mo 79b) D. M. Moltz, Lawrence Berkeley Laboratory Report LBL-9718, Ph. D. Thesis, unpublished (1979).

(Mo 80a) D. M. Moltz, R. A. Gough, M. S. Zisman, D. J. Vieira, H. C. Evans and J. Cerny, Nucl. Instr. Meth. 172, 507 (1980).

(Mo 80b) D. M. Moltz, J. M. Wouters, J. Äystö, M. D. Cable, R. F. Parry, R. D. von Dincklage and J. Cerny, Nucl. Instr. Meth. 172, 519 (1980).

(Mo 80c) P. Möller and J. Nix, Los Alamos National Laboratory Report, LA-UR-80-1996 (1980).

(Mo 81a) D. M. Moltz, J. Äystö, M. D. Cable, R. F. Parry, P. E. Haustein, J. M. Wouters and J. Cerny, Nucl. Instr. Meth. 186, 141 (1981).

(Mo 81b) P. Möller and J. R. Nix, Nucl. Phys. A361, 117 (1981).

(My 66a) W. D. Myers and W. J. Swiatecki, Nucl. Phys. 81, 1 (1966).

(My 66b) W. D. Myers and W. J. Swiatecki, Arkiv For Fysik 36, 343 (1966).

(My 69) W. D. Myers and W. J. Swiatecki, Ann. Phys. 55, 395 (1969).

(My 71) W. D. Myers, in Dynamic Structure of Nuclear States, edited by D. Rowe, L. Trainor, S. Wong and T. Donnelley (University of Toronto Press, Toronto, Canada) p. 233 (1971).

(My 74) W. D. Myers and W. J. Swiatecki, Ann. Phys. 84, 186 (1974).

(My 77) W. D. Myers, Droplet Model of Atomic Nuclei, (Plenum Press, New York, 1977).

(Ne 74) Bulletin on Plastic Scintillators, Nuclear Enterprises Inc. (San Carlos, California, 1974).

(Ni 61) S. G. Nilsson and O. Prior, K. Dan. Vidensk. Selsk. Mat. Fys. Medd. 32, No. 16 (1961).

(Ot 79) H. Otto, P. Peuser, G. Nyman and E. Roeckl, Nucl. Instr. Meth. 166, 507 (1979).

(Pa 78) R. C. Pardo, E. Kashy, W. Benenson and L. W. Robinson, Phys. Rev. C18, 1249 (1978).

(Pl 79) A. Plochocki, G. M. Gowdy, P. Kirchner, O. Klepper, W. Reisdorf, E. Roeckl, P. Tidemand-Petersson, J. Zylicz, U. J. Schrewe, R. Kantus, R. D. von Dincklage and W. D. Shimdt-Ott, Nucl. Phys. A332, 29 (1979).

(Pl 81) A. Plochocki, J. Zylicz, R. Kirchner, O. Klepper, E. Roeckl, P. Tidemand-Petersson, I. S. Grant, P. Misaelides, and W. D. Schmidt-Ott, in Proceedings of the Fourth International Conference on Nuclei Far From Stability, June 7-13, Helsingor, Denmark, (CERN report 81-09), p. 163.

(Ra 76) H. L. Ravn, L. C. Carraz, J. Denimal, E. Kugler, M. Skarestad, S. Sundell and L. Westgaard, Nucl. Instr. Meth. 139, 267 (1976).

(Ra 79) H. L. Ravn, Phys. Rep. 54, 201 (1979).

(Re 78) D. M. Rehfield, Nucl. Instr. Meth. 157, 351 (1978).

(Ro 65) P. C. Rogers and G. E. Gordon, Nucl. Instr. Meth. 37, 259 (1965).

(Ro 78) F. Rösel, H. M. Fries, K. Alder and H. C. Pauli, At. Data and Nucl. Data Tables 21, 92 (1978).

(Sc 76) H. Schmeing, V. Koslowsky, M. Wightman, J. C. Hardy, J. A. MacDonald, T. Faestermann, H. R. Andrews, J. S. Geiger and R. L. Graham, Nucl. Instr. Meth. 139, 335 (1976).

(Sc 79) K. H. Schmidt, W. Faust, G. Munzenberg, H. G. Clerc, W. Lang, K. Pielenz, D. Vermeulen, H. Wohlfarth, H. Ewald and K. Guttner, Nucl. Phys. A318, 253 (1979).

(Sc 80) K. H. Schmidt and D. Vermeulen, in Proceedings of the Sixth International Conference on Atomic Masses and Fundamental Constants, edited by J. A. Nolen, Jr. and W. Benenson, (Plenum Press, New York, 1980) p. 119.

(Se 73) R. G. Sextro, Lawrence Berkeley Laboratory Report LBL-2360, Ph. D. Thesis, unpublished (1973).

(Se 75) P. A. Seeger and W. M. Howard, Nucl. Phys. A238, 491 (1975).

(Se 77) E. Segré, Nuclei and Particles, 2nd ed., (W. A. Benjamin Inc., Reading, Massachusetts, 1977) p. 391.

(Se 78) K. K. Seth, H. Nann, S. Iversen, M. Kaletka and J. Hird, Phys. Rev. Lett. 41, 1589 (1978).

(Sh 74) A. DeShalit and H. Feshbach, Theoretical Nuclear Physics, vol. 1, (John Wiley and Sons Inc., New York, 1974) p. 771.

(Si 69) G. Sidenius, in Prodceedings of the First International Conference on Ion Sources, Saclay, France, p. 401 (1969).

(So 71) R. A. Sorensen, Phys. Lett. 34B, 21 (1971).

(St 67) V. M. Strutinsky, Nucl. Phys. A95, 420 (1967).

(Sw 64) W. J. Swiatecki, in Proceedings of the Conference on Nuclidic Masses, 2nd ed., edited by W. H. Johnson, Jr., (Springer-Verlag, New York, 1964) p. 58.

(Th 75) C. Thibault, R. Klapisch, C. Rigaud, A. M. Poskanzer, R. Prieels, L. Lessard and W. Reisdorf, Phys. Rev. C12, 644 (1975).

(Th 78) C. E. Thorn, P. D. Bond, M. J. Levine, W. F. Piel and A. Gallmann, BAPS 23, 72 (1978).

(Ti 81) P. Tidemand-Petersson, R. Kirchner, O. Klepper, W. Kurcewicz, E. Roeckl and E. F. Zganjar, Z. Physik A302, 343 (1981).

(Tr 81) J. Tréherne, R. Béraud, A. Charvet, R. Duffait, J. Genevey and M. Meyer, in Proceedings of the Fourth International Conference on Nuclei Far From Stabibility, June 7-13, 1981, Helsingor, Denmark, (CERN report 81-09), p. 459.

(Vi 78) D. J. Vieira, Lawrence Berkeley Laboratory Report LBL-7161, Ph. D. Thesis, unpublished (1978).

(Vi 80) D. J. Vieira, G. W. Butler, L. P. Remsberg, A. M. Poskanzer and H. Wollnik, attachment 20.1.3 Los Alamos Scientific Laboratory (internal report) (1980).

(von W 35) C. F. von Weizäcker, Z. Physik 96, 431 (1935).

(Wa 54) K. Way and M. Wood, Phys. Rev. 94, 119 (1954).

(Wa 77) A. H. Wapstra and K. Bos, At. Data and Nucl. Data Tables 19, 177 (1977).

(We 75) C. Weiffenbach, S. C. Gujrathi, J. K. P. Lee and A. Houdayer, Nucl. Instr. Meth. 125, 245 (1975).

(Wi 57) E. P. Wigner, Proceedings of the Robert A. Welch Conferences on Chemical Research, Houston, Texas, November 20-22, 1957, vol. 1, p. 67.

(Wi 80) I. N. Wischnewski, H. V. Klapdor, P. Herges, H. Fromm and W. A. Zheldonozhski, Z. Physik A298, 21 (1980).

(Wo 72) F. K. Wohn, J. R. Clifford, G. H. Carlson and W. L. Talbert, Jr., Nucl.Instr. Meth. 101, 343 (1972).

(Wo 76) H. Wollnik, Nucl. Instr. Meth. 139, 311 (1976).

(Wo 81a) Computer code SPECTR written by J. M. Wouters (1981).

(Wo 81b) Computer code PHOTO2 written by J. M. Wouters (1981).

(Wo 82) J. M. Wouters, H. M. Thierens, J. Äystö, M. D. Cable, P. E. Haustein, R. F. Parry and Joseph Cerny, to be published in Phys. Rev. C (1982).

(Wu 66) C. S. Wu and S. A. Moskowski, Beta Decay, (Interscience Publishers, New York, 1966) chapters 1-3.

(Ze 80) N. Zeldes, Proceedings of the Sixth International Conference on Atomic Masses and Fundamental Constants, edited by J. A. Nolen, Jr. and W. Benenson (Plenum Press, New York, 1980) p. 129.

(Ze 81) N. Zeldes, Proceedings of the Fourth International Conference on Nuclei Far From Stability, June 7-13, 1981, Helsingor, Denmark, (CERN report 81-09), p. 93.

(Zi 74) J. P. Zirnheld, Nucl. Instr. Meth. 120, 171 (1974).